Comparison of Two-Moment Bulk Microphysics Schemes in Idealized Supercell Thunderstorm Simulations

HUGH MORRISON

National Center for Atmospheric Research,* Boulder, Colorado

JASON MILBRANDT

Numerical Weather Prediction Research Section, Meteorological Research Division, Environment Canada, Dorval, Quebec, Canada

ABSTRACT

Idealized three-dimensional supercell simulations were performed using the two-moment bulk microphysics schemes of Morrison and Milbrandt–Yau in the Weather Research and Forecasting (WRF) model. Despite general similarities in these schemes, the simulations were found to produce distinct differences in storm structure, precipitation, and cold pool strength. In particular, the Morrison scheme produced much higher surface precipitation rates and a stronger cold pool, especially in the early stages of storm development. A series of sensitivity experiments was conducted to identify the primary differences between the two schemes that resulted in the large discrepancies in the simulations.

Different approaches in treating graupel and hail were found to be responsible for many of the key differences between the baseline simulations. The inclusion of hail in the baseline simulation using the Milbrant–Yau scheme with two rimed-ice categories (graupel and hail) had little impact, and therefore resulted in a much different storm than the baseline run with the single-category (hail) Morrison scheme. With graupel as the choice of the single rimed-ice category, the simulated storms had considerably more frozen condensate in the anvil region, a weaker cold pool, and reduced surface precipitation compared to the runs with only hail, whose higher terminal fall velocity inhibited lofting. The cold pool strength was also found to be sensitive to the parameterization of raindrop breakup, particularly for the Morrison scheme, because of the effects on the drop size distributions and the corresponding evaporative cooling rates. The use of a more aggressive implicit treatment of drop breakup in the baseline Morrison scheme, by limiting the mean–mass raindrop diameter to a maximum of 0.9 mm, opposed the tendency of this scheme to otherwise produce large mean drop sizes and a weaker cold pool compared to the hail-only run using the Milbrandt–Yau scheme.

1. Introduction

The parameterization of cloud and precipitation microphysics is a major challenge in the numerical simulation of moist deep convection. Microphysical processes directly impact buoyancy, and hence convective fluxes, through condensate loading and latent heating/cooling due to phase changes. The representation of these effects is becoming increasingly important since regional-scale numerical weather prediction (NWP) models are now commonly run at the deep-convective scale, with a horizontal grid spacing of the order of 1 km (Kain et al. 2008; Lean et al. 2008).

Current models generally use bulk microphysics schemes (BMSs) to parameterize the effects of cloud microphysical processes, although detailed bin microphysics schemes are being increasingly used in research models (e.g., Khain et al. 2004). In a BMS, the hydrometeors are partitioned into several particle categories for which an analytic form of the particle size distribution (PSD) is assumed and one or more bulk quantities related to moments of the PSD are predicted. With the exception of the two-moment scheme of Koenig and Murray (1976), most of the earlier BMSs were single moment, predicting only the mixing ratio for each species (e.g., Kessler 1969; Rutledge and Hobbs 1983; Lin et al. 1983; Walko et al. 1995; Kong and

Yau 1997). Two-moment schemes were later developed, where both the mixing ratio and total number concentration of at least one species was predicted (e.g., Ziegler 1985; Cotton et al. 1986; Murakami 1990; Ferrier 1994; Meyers et al. 1997; Reisner et al. 1998; Cohard and Pinty 2000; Seifert and Beheng 2001; Milbrandt and Yau 2005b; Morrison et al. 2005; Phillips et al. 2007). The prediction of two independent moments allows for greater flexibility in representing the evolution of the PSD and thus, in principle, an improved capacity to simulate microphysical processes. It will be shown in this paper, however, that considerable sensitivity to specific aspects of these schemes remains.

The use of two-moment schemes has become increasingly common for the simulation of organized deep convection using convective-scale models (Ferrier et al. 1995; Meyers et al. 1997; Milbrandt and Yau 2006, hereafter MY06; Morrison et al. 2009, hereafter MTT09; Luo et al. 2010; Dawson et al. 2010, hereafter D10). Key processes that are strongly affected by using the two-moment approach include melting, evaporation, collection, and particle size sorting. For example, MTT09 and Luo et al. (2010) found that a two-moment scheme reduced rain evaporation in the trailing stratiform region of a squall line relative to using a one-moment version of the same scheme, leading to increased stratiform precipitation at the surface, a weakened cold pool, and more realistic vertical profile of radar reflectivity. Similarly, more realistic supercell simulations, compared to observations, were obtained by MY06 and D10 with a two-moment BMS compared to the one-moment version of the same scheme. Mansell (2008) also showed better representation of cold pool structure and forward-flank reflectivity using two-moment compared to one-moment schemes in an ensemble Kalman filter study.

Despite improvements in simulations using two-moment schemes, there still remains a great deal of uncertainty in the parameterization of several specific processes in BMSs in general, from which two-moment schemes are not immune. For the treatment of the ice phase, the standard approach is to partition the frozen hydrometeors into different categories, each with common bulk characteristics, in an attempt to represent the wide range of observed particle types. However, the appropriate number and type of ice-phase categories is unclear. There has been some examination on the sensitivity of the number of ice-phase categories in bulk schemes (e.g., Fovell and Ogura 1988; McCumber et al. 1991; Ferrier et al. 1995) which generally indicate that the realism of simulated storms systems increases with the number of ice-phase categories, at least to the extent that the addition of categories with different bulk characteristics serves to improve the overall representation of the large range of observed particles. On the other hand, the paradigm of including different classes of ice with fixed characteristics may lead to uncertainty given

that in nature ice particles exhibit a continuum of characteristics (cf. Morrison and Grabowski 2008).

The evaporation of rain plays an important role in determining the cold pool strength which in turn affects the storm dynamics associated with intense continental convection (Gilmore and Wicker 1998). Thus, the simulation of deep convection is sensitive to the treatment of the PSD of rain. While two-moment schemes have an additional degree of freedom, it is still unclear how to best parameterize processes such as drop breakup and the shedding of liquid water from the surface of graupel/hail during accretion and melting, both of which affect the shape of the rain PSD and thus the evaporative cooling rates.

Furthermore, the appropriate values of many parameters in a BMS are often uncertain, yet simulations can be very sensitive to the specific settings. For example, Gilmore et al. (2004) and Van Weverberg et al. (2010) showed large sensitivity of simulated supercell storm dynamics and precipitation to changes in the assumed bulk density and fixed intercept parameter of the graupel/hail category using single-moment BMSs. Similarly, van den Heever and Cotton (2004) and Cohen and McCaul (2006) showed sensitivity of supercell storms to changes in specified mean graupel/hail particle size in a single-moment scheme, although Cohen and McCaul (2006) found limited sensitivity of surface precipitation. While two-moment schemes are not constrained to specify (or diagnose) the intercept parameter or mean particle size, the sensitivity to the specification of other quantities related to the rimed-ice category, such as bulk density or fall velocity parameters, has not been examined in the context of these schemes. Given that two-moment schemes can behave much differently than one-moment schemes for the simulation of deep convection (e.g., MY06; MTT09; D10), one cannot simply extrapolate the results from one-moment studies to give the expected behavior of two-moment schemes in terms of these sensitivities.

To this end, the impacts of using the two-moment BMSs of MTT09 and Milbrandt and Yau (2005a,b), hereafter MOR and MY schemes, respectively, in simulations of deep convective storms within a common modeling framework are examined. Specifically, this study seeks 1) to compare the behavior of the baseline configurations of the MOR and MY schemes for simulations of an idealized supercell thunderstorm where all other model conditions are identical, and 2) to examine, through sensitivity tests, the primary reasons for the discrepancies between the baseline simulations. The main focus is on differences in the representation of graupel and hail and the treatment of raindrop breakup, which were found in this study to account for some of the key differences in the simulated storm structure, surface precipitation, and cold pool characteristics between the MOR and MY baseline simulations.

TABLE 1. List of the main simulations.

Simulation	Description
MOR-BASE	Baseline run (MOR)
MOR-GRPL	Parameters of the single rime ice category representative of medium-density graupel in MOR
MOR-BASE-V	Same as MOR-BASE except for MY V–D parameters for rain and hail
MOR-GRPL-V	Same as MOR-GRPL except for MY V–D parameters for rain
MOR-HV	Same as MOR-BASE except for bulk density of hail set to that graupel
MOR-GV	Same as MOR-GRPL except for bulk density of graupel set to that of hail
MOR-BRK_Z	Same as MOR-BASE-V except for rain drop breakup following Ziegler (1985)
MOR-BRK_VC	Same as MOR-BASE-V except for rain drop breakup following Verlinde and Cotton (1993)
MOR-BRK_S	Same as MOR-BASE-V except for rain drop breakup following Seifert (2008)
MOR-DMR5	Same as MOR-BASE-V except that $D_{\mathrm{mr\_max}} = 5$ mm
MY-BASE	Baseline run (MY)
MY-GRPL	Graupel only (hail category shut off in MY)
MY-HAIL	Hail only (graupel category shut off in MY)
MY-DMR5	Same as MY-HAIL except Ziegler (1985) rain drop breakup is turned off
MY-DMR0.9	Same as MY-DMR5 except that $D_{\mathrm{mr\_max}} = 0.9$ mm
MY-BRK_VC	Same as MY-HAIL except for rain drop breakup following Verlinde and Cotton (1993)
MY-BRK_S	Same as MY-HAIL except for rain drop breakup following Seifert (2008)

The paper is organized as follows. Section 2 gives a brief description of the numerical model. Section 3 describes the case and model setup. Results are presented in section 4. Concluding remarks are given in section 5.

2. Model description

All of the simulations in this study were conducted using the Advanced Research Weather Research and Forecasting model (ARW-WRF) version 3.1 (Skamarock et al. 2007), which is a compressible, nonhydrostatic, three-dimensional (3D) mesoscale model. The governing equations are solved using a time-split integration with the third-order Runge–Kutta scheme.

Horizontal and vertical turbulent diffusion are calculated using a 1.5-order turbulent kinetic energy (TKE) scheme (Skamarock et al. 2007). Horizontal and vertical advection are calculated using fifth- and third-order discretization schemes, respectively, with a limiter to ensure positive definiteness (Skamarock et al. 2007). The upper and lower boundaries are free slip with zero vertical velocity. For all of the simulations discussed in this paper, surface fluxes were set to zero and radiative transfer has been neglected for simplicity. The MOR and MY schemes, as used in this study, are described in the appendix.

3. Experimental design

An idealized supercell storm using simplified boundary conditions is simulated. Two baseline simulations are performed, one for each BMS. A set of sensitivity experiments is then conducted in order to determine the specific differences in the two schemes that resulted in differences between the respective baseline runs (Table 1).

The case set up for this study is similar to the standard 3D idealized supercell case available as part of the WRF modeling system. Boundary conditions are open on all lateral boundaries. Horizontal and vertical grid spacings are 1 km and approximately 500 m, respectively. The primary model time step is 6 s with 1-s subtime steps used for the acoustic modes. The domain size is 200×200 km^2 in the horizontal with the model lid at 20 km. A Rayleigh damper with damping coefficient of 0.003 s^{-1} is used in the upper 5 km to damp waves in the stratosphere. The model is initialized with the analytic sounding of Weisman and Klemp (1982; 1984). The melting level is located at a height of approximately 4 km. These simulations use the quarter-circle supercell hodograph of Weisman and Rotunno (2000, see their Fig. 3b), except that the shear is extended to a height of 7 km (as in the idealized quarter-circle supercell test case available in WRF) instead of 6 km. This hodograph features a quarter-circle shear from the surface to 2 km and unidirectional shear above 2 km, with a length of 40 m s^{-1}. Convection is triggered using a thermal perturbation with maximum perturbation potential temperature θ of 3 K centered at a height of 1.5 km and varying as the cosine squared to the edge, with a horizontal radius of 10 km and a vertical radius of 1.5 km. All simulations are integrated for 2 h.

Tests with other horizontal and vertical grid spacings were performed and resulted in some differences in the simulations. For example, reducing the horizontal and
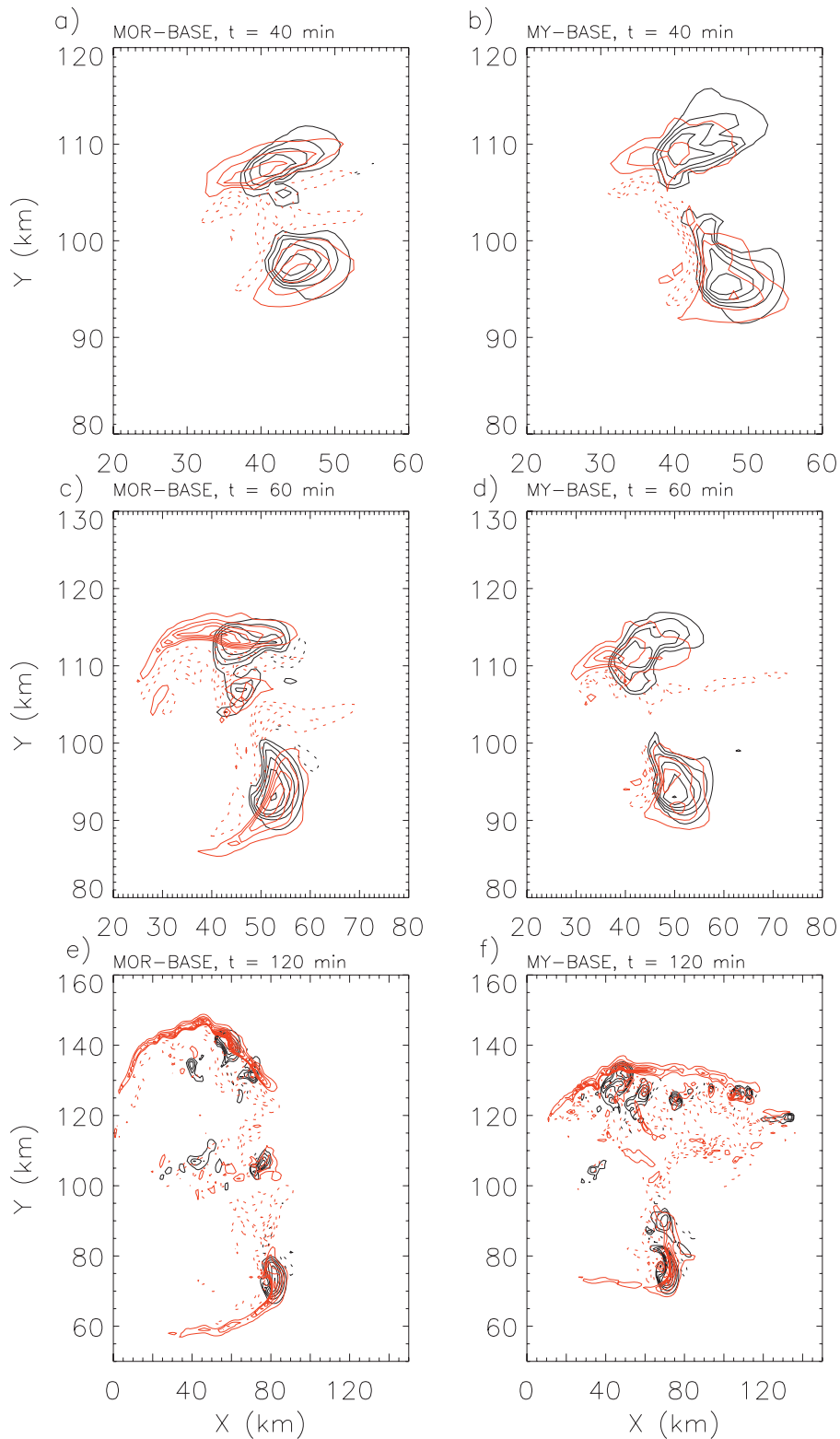
FIG. 1. Vertical air velocity at heights of ~0.75 km (red contours) and ~4.7 km (black contours) for MOR-BASE at time t = (a) 40, (c) 60, and (e) 120 min, and MY-BASE at t = (b) 40, (d) 60, and (f) 120 min. Red (black) contours indicate 1 (5) m s^{-1} intervals, with zero contours not shown. Upward velocities are indicated by the solid line and downward velocities are indicated by the dotted line.
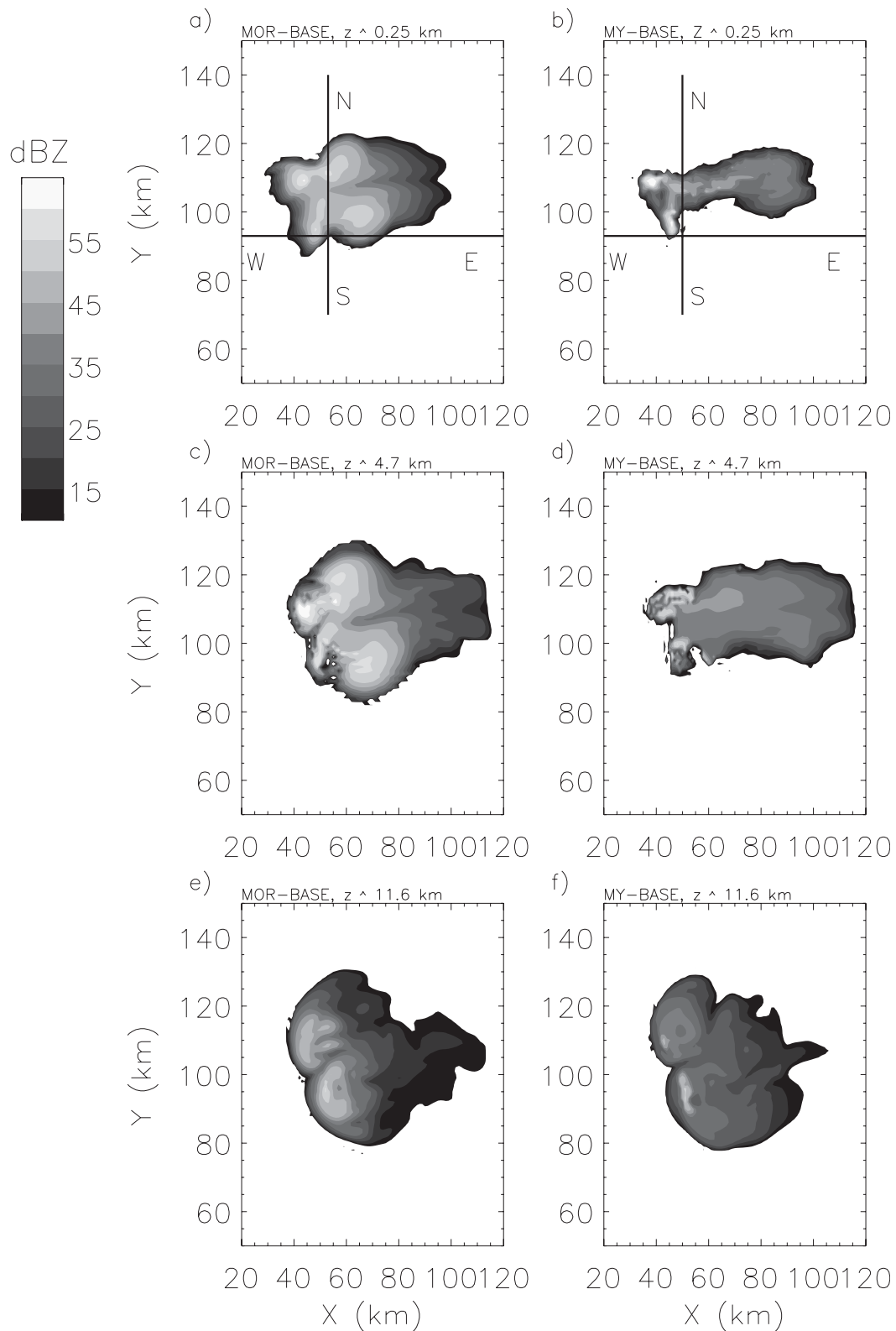
FIG. 2. Horizontal cross sections of radar reflectivity at time t = 60 min for MOR-BASE at height (a) ~0.25, (c) ~4.7, and (e) ~11.6 km, and MY-BASE at height (b) ~0.25, (d) ~4.7, and (f) ~11.6 km. Lines shown in (a) and (b) indicate locations of the vertical cross sections shown in Figs. 4 and 5.
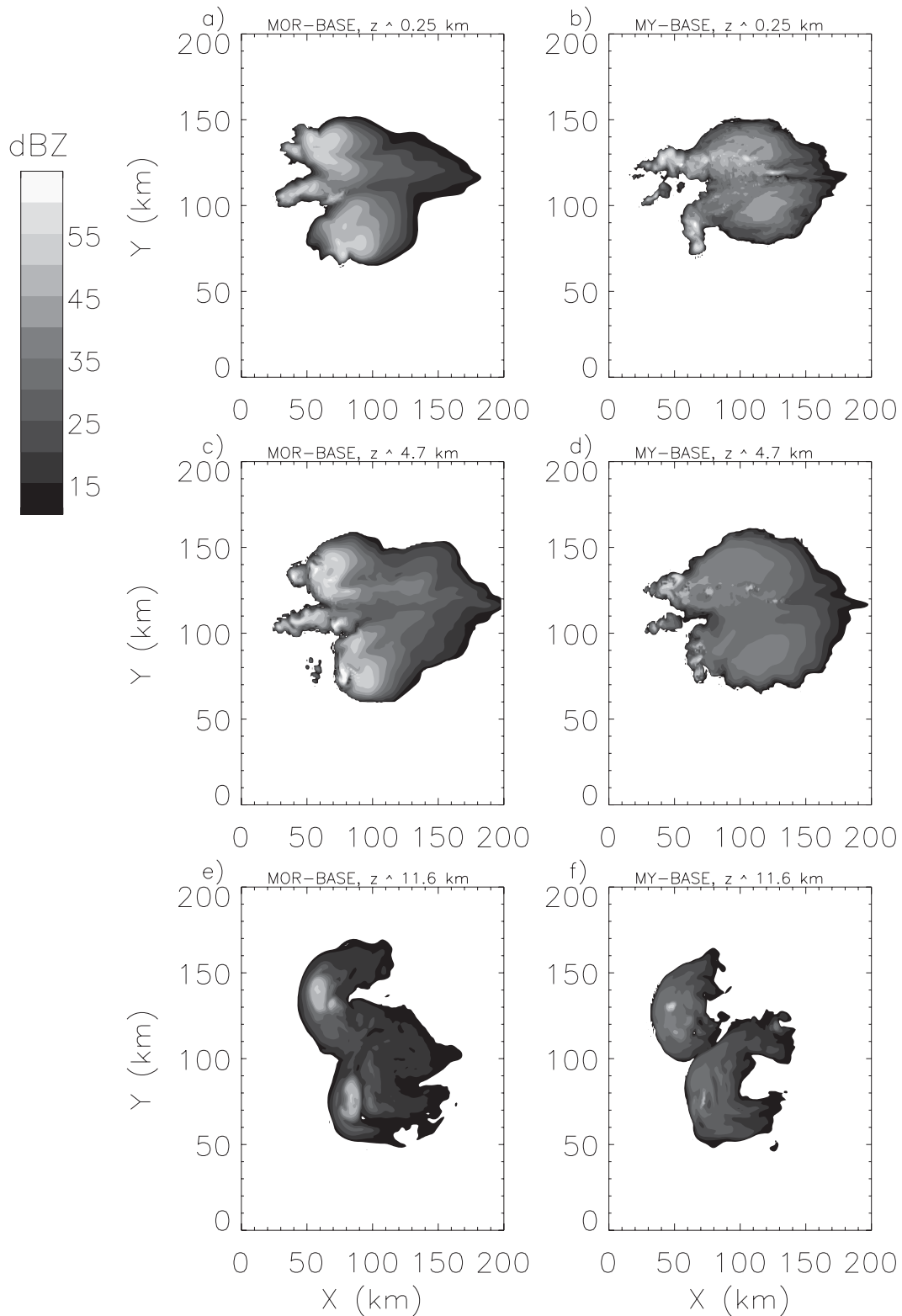
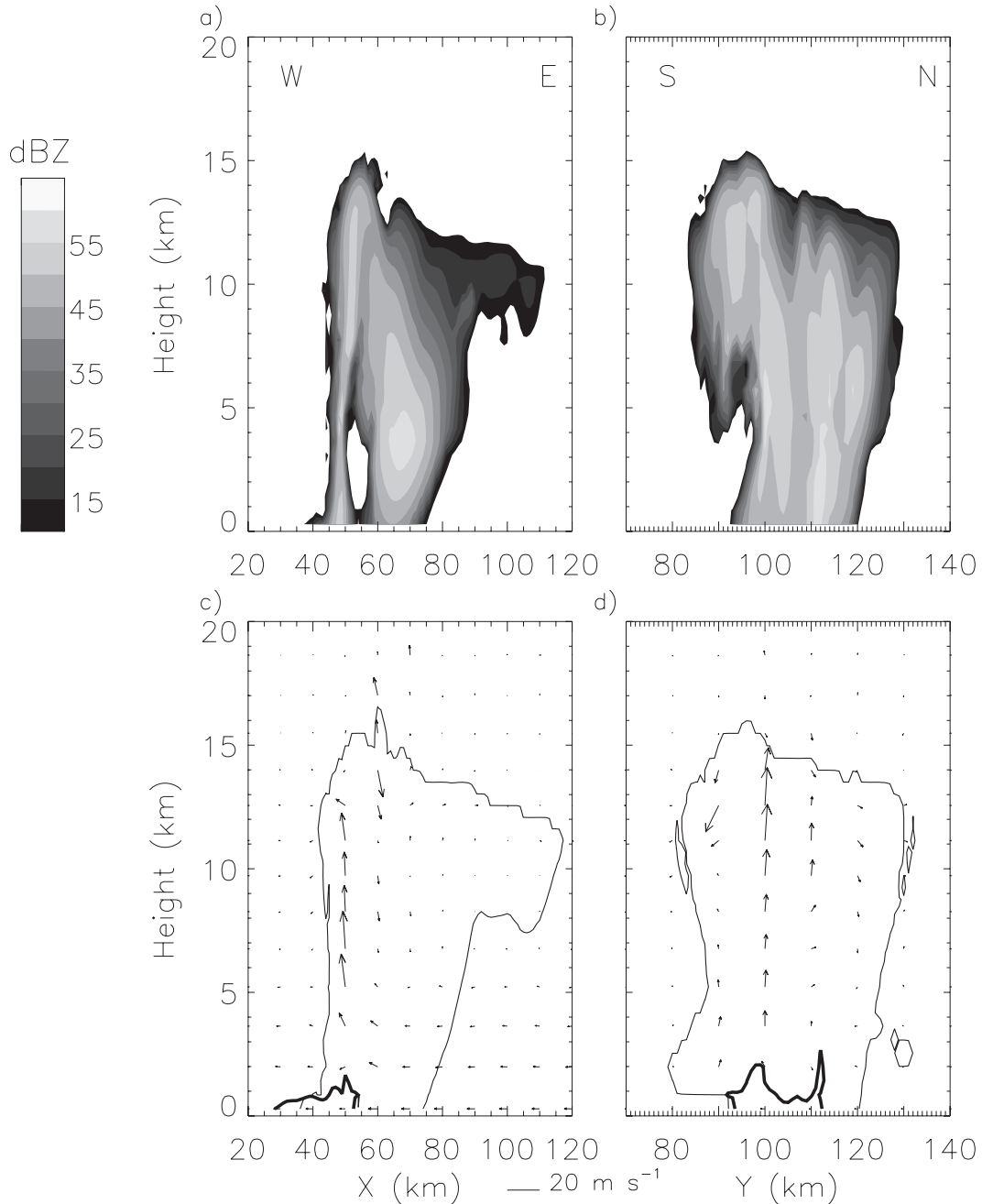Fig. 3. As in Fig. 2, but for radar reflectivity at time t = 120 min.

FIG. 4. Vertical cross sections of radar reflectivity at $t = 60$ min in the (a) x–z, and (b) y–z planes, and 2D wind vectors, hydrometeor boundary defined by a threshold mixing ratio of 0.001 g kg^{-1} (thin line), and cold pool boundary defined by the -2-K perturbation potential temperature isotherm (thick line) along the (c) x–z and (d) y–z planes for MOR-BASE. Locations of the W–E and S–N transects in the horizontal x–y plane are shown in Fig. 2a. Wind vectors are relative to the environmental wind above 7 km of 27.5 m s^{-1} in the x direction and are plotted every 10 km.

vertical grid spacing by a factor of 2 led to a 1–2-K reduction of minimum low-level θ; however, overall differences between the MOR and MY simulations were similar. Thus, we are satisfied that the model configuration described above, which was identical for all runs described in this paper, is adequate to conduct meaningful sensitivity experiments and to analyze differences produced by the microphysics schemes. Detailed investigation of sensitivity to resolution and other aspects of model configuration are left for future work.
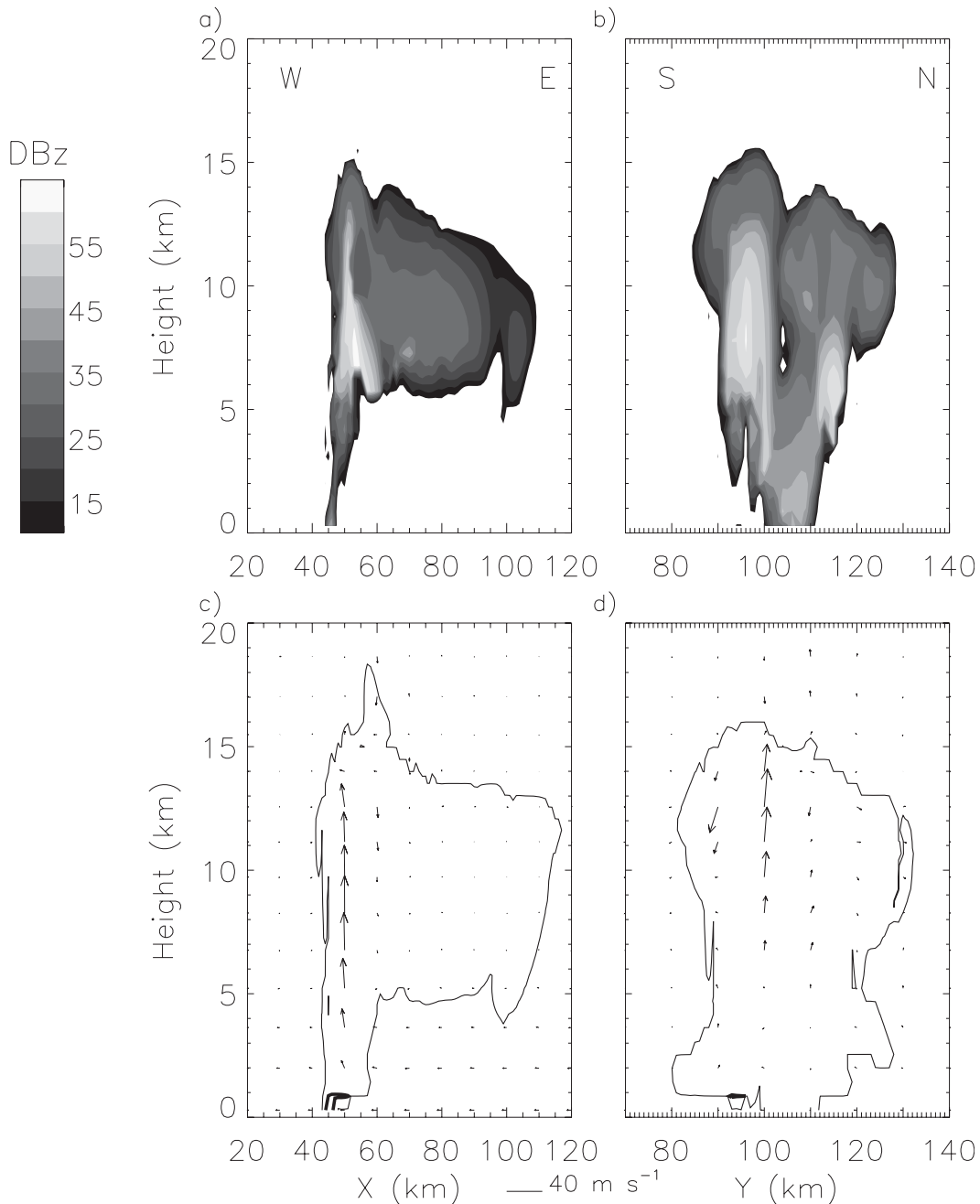
FIG. 5. As in Fig. 4, but for MY-BASE. Locations of the W–E and S–N transects in the horizontal x–y plane are shown in Fig. 2b.

4. Baseline simulations

a. Storm structure and radar reflectivity

Horizontal cross sections of vertical velocity w and radar reflectivity Z at different heights z and times are shown in Figs. 1–3. Vertical cross sections of Z, wind vectors, and hydrometeor and cold pool boundaries at simulation time $t = 60$ min (along the west–east and south–north transects

in Fig. 2) are shown in Figs. 4–5. These transects are centered near the location of the maximum updraft velocity associated with the right-moving storm cell in each simulation.

Storm characteristics in approximately the first 30 min of the two simulations are similar and dominated by the environmental sounding, shear, and initial thermal perturbation. Precipitation processes then become important and
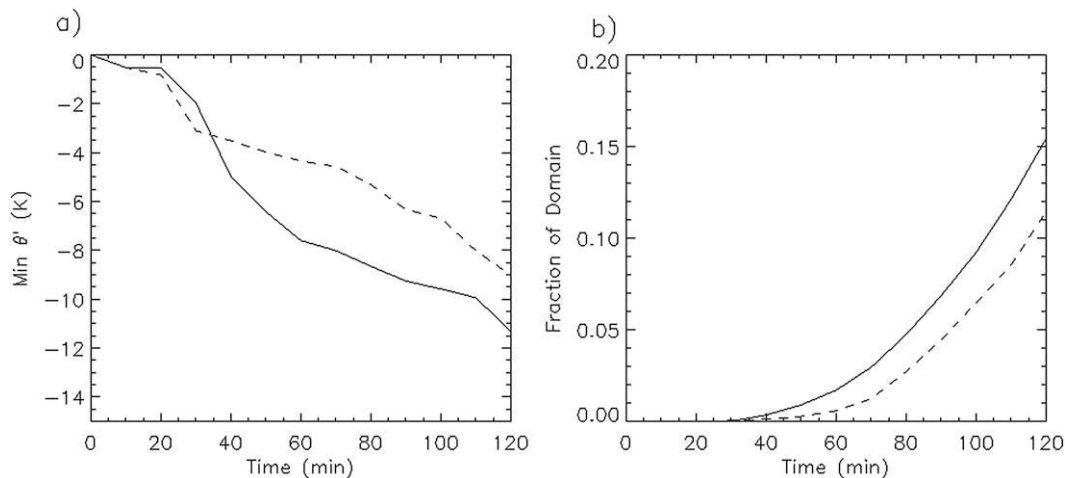
FIG. 6. Time evolution of (a) minimum low level ($z \sim 0.25$ km) θ' and (b) fraction of domain area with low-level cold pool defined by the -2-K θ' isotherm for MOR-BASE (solid) and MY-BASE (dotted).

differences between MOR and MY schemes begin to produce different dynamic and thermodynamic storm characteristics. In both MOR-BASE and MY-BASE, splitting into left- and right-moving storms begins around $t = 30$ min. While overall storm splitting is similar in height and timing, MY-BASE has upward motion at low- and midlevels between the left- and right-moving cells and a fairly distinct rear-flank downdraft at low levels (Fig. 1b), while MOR-BASE has low-level downward motion between the cells and greater low-level convergence and hence stronger upward motion aligned along the axis of

midlevel ascent associated with the two primary storm cells (Fig. 1a).

The two simulations further diverge in time as the precipitation and cold pools evolve. Strong low-level convergence and upward motion along the rear flank of the right- and left-moving cells occurs in MOR-BASE (Figs. 1c,e). In contrast, a stronger forward-flank downdraft is evident in MY-BASE, with low-level convergence along the edge of the forward-flank downdraft producing a secondary line of convective cells aligned with the primary left-moving storm (Fig. 1f). By $t = 120$ min,

TABLE 2. Domain-average accumulated surface precipitation, minimum low-level ($z \sim 250$ m) θ', and fraction of domain area with low-level cold pool defined by the -2-K θ' isotherm for the main simulations at time $t = 60$ and 120 min.

| Simulation	$t = 60$ min			$t = 120$ min		
	Accumulated precipitation (mm)	Min θ' (K)	Cold pool fraction	Accumulated precipitation (mm)	Min θ' (K)	Cold pool fraction
MOR-BASE	0.14	−7.60	0.017	1.28	−11.32	0.154
MOR-GRPL	0.04	−3.78	0.004	0.46	−6.70	0.053
MOR-HV	0.12	−4.26	0.006	1.11	−7.89	0.080
MOR-GV	0.04	−3.50	0.004	0.37	−4.67	0.033
MOR-BASE-V	0.10	−5.51	0.010	0.95	−8.94	0.117
MOR-GRPL-V	0.05	−3.95	0.005	0.47	−6.11	0.045
MOR-BRK_Z	0.13	−2.81	0.003	1.09	−6.65	0.051
MOR-BRK_VC	0.13	−3.65	0.004	1.13	−6.14	0.044
MOR-BRK_S	0.10	−4.52	0.006	0.97	−7.62	0.075
MOR-DMR5	0.14	−1.93	0.000	1.18	−3.46	0.006
MY-BASE	0.04	−4.35	0.006	0.41	−9.03	0.114
MY-GRPL	0.04	−4.57	0.006	0.48	−9.84	0.122
MY-HAIL	0.10	−7.38	0.015	1.01	−10.26	0.167
MY-DMR5	0.12	−4.46	0.014	1.07	−9.89	0.147
MY-DMR0.9	0.07	−9.11	0.022	0.89	−11.40	0.190
MY-BRK_VC	0.11	−7.61	0.014	1.04	−10.05	0.162
MY-BRK_S	0.09	−8.57	0.016	0.96	−10.03	0.172
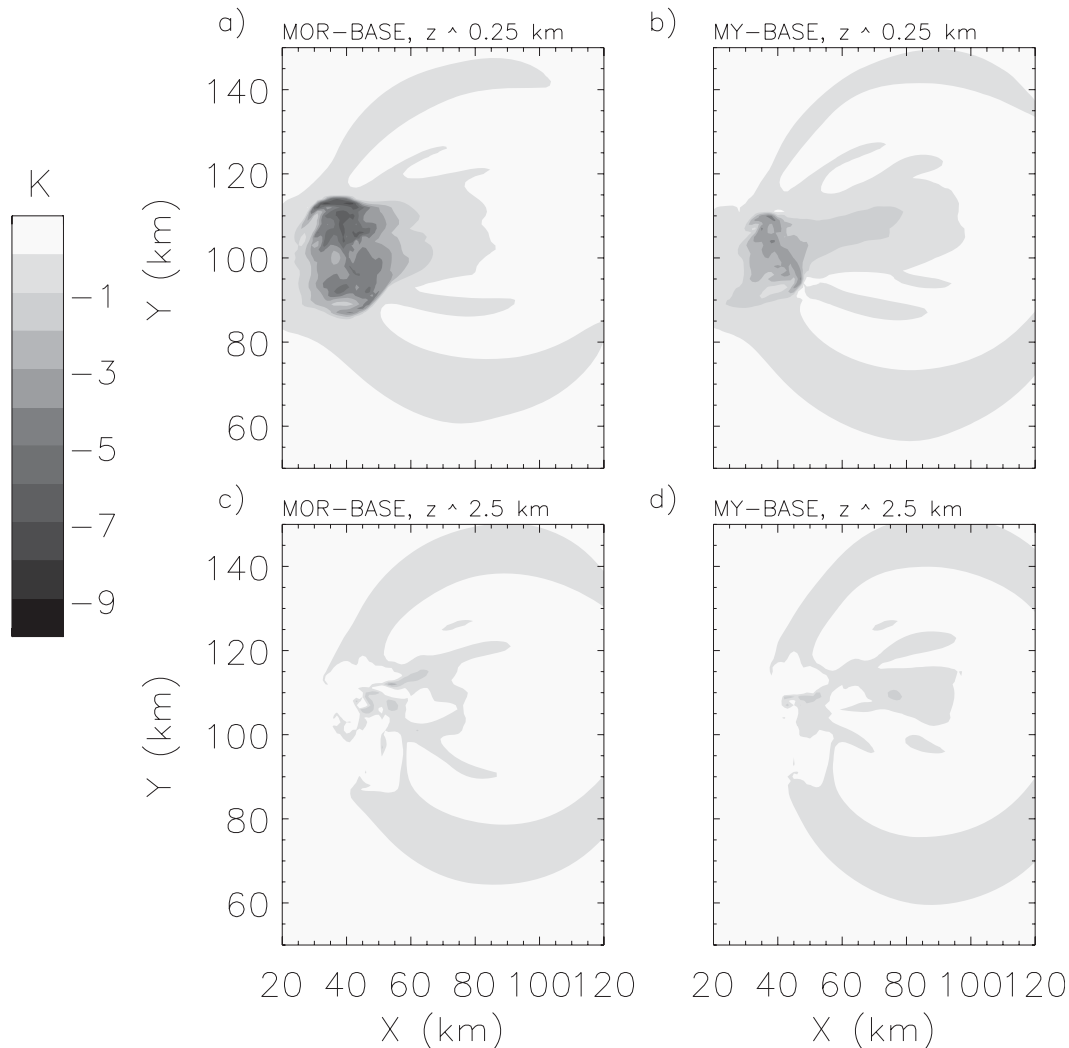
FIG. 7. Horizontal cross sections of perturbation potential temperature at time $t = 60$ min for MOR-BASE at height (a) ~0.25 and (c) 2.5 km, and for MY-BASE at height (b) ~0.25 and (d) 2.5 km.

the primary right- and left-moving cells are located about 55 km apart in MY-BASE. In MOR-BASE, the cells are about 70 km apart, with a line of secondary convection associated with low-level convergence between the primary left- and right-moving cells (Fig. 1e).

The magnitudes of Z through most of the depth of the storm are larger in the vicinity of the primary cells in MOR-BASE (Figs. 2–3), which is associated with greater amounts of hail and rain. Both schemes also produce extensive precipitation in the forward-flank region with Z values near the surface greater than 10 dBZ extending 50 km from the primary storm cells at $t = 60$ min (Figs. 2a,b), and extending over 100 km at $t = 120$ min (Figs. 3a,b). The Z values are larger at low- and midlevels in the forward-flank region in MY-BASE at greater distances (>30–40 km) from the primary cells. MY-BASE has an especially long and narrow

forward flank, particularly at earlier times in the simulation. This is consistent with the findings of D10 using the MY scheme. The noisy appearance in the Z field in MY-BASE at low- and midlevels in the forward-flank region at $t = 120$ min (Figs. 3b,d) is associated with localized pockets of large hail produced by fairly intense secondary convective cells along the line of low-level convergence at the edge of the forward-flank downdraft (see Fig. 1f).

Large differences between the runs are evident in the vertical cross sections of Z (Figs. 4–5), with much larger values in MOR-BASE in the vicinity of the right-moving storm, particularly below the freezing level (at $z \sim 4$ km). However, the peak values are larger in MY-BASE. There is also a more distinct bounded weak echo region in MOR-BASE and a more extensive cold pool downshear of the midlevel updraft. Both schemes produce other
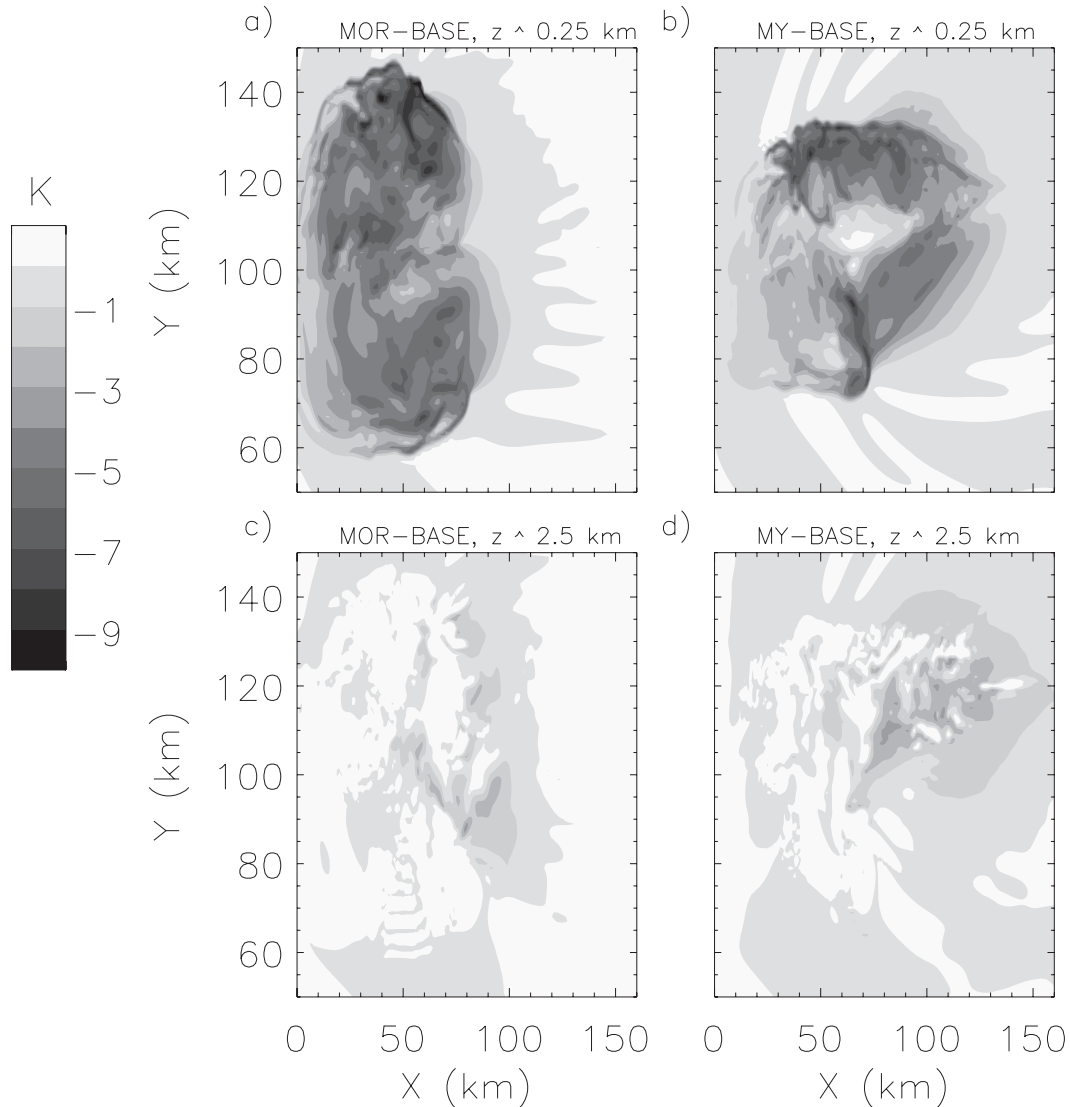
FIG. 8. As in Fig. 7, but at time $t = 120$ min.

classic features of supercell storms, such as the shelf clouds indicated by the cross section of hydrometeor boundaries (Figs. 4d and 5d).

b. Cold pool and dynamics

After $t = 35$ min, MOR-BASE has a much colder and more extensive cold pool than MY-BASE (Fig. 6 and Table 2), where the cold pool is defined by the less than −2-K perturbation potential temperature θ' region. The difference in minimum θ' near the surface ($z \sim 0.25$ km) between the simulations exceeds 3 K at $t = 60$ min, decreasing somewhat after this time. For comparison, in MY06 and D10 differences in θ' of 3–5 K were produced by one-moment and two-moment versions of the MY scheme for supercell simulations. Large differences between

MOR-BASE and MY-BASE are also apparent in terms of equivalent potential temperature, θ_e (not shown), suggesting that cold pool air descends from higher altitude (i.e., lower θ_e) in MOR-BASE, assuming that θ_e is approximately conserved in downdrafts. This is also consistent with D10, who found that the stronger the cold pool, the higher the levels that the parcels originated.

Specific differences in θ' between the simulations depend on height and location relative to storm features (Figs. 7–8). At low levels ($z \sim 0.25$ km), MOR-BASE is colder than MY-BASE in the region near the updraft cores, where the heaviest precipitation is concentrated, and along the rear flanks of the right- and left-moving storms (Figs. 7a,b and 8a,b). In contrast, MY-BASE is colder in the forward-flank region, especially later in the simulation as indicated by θ' at
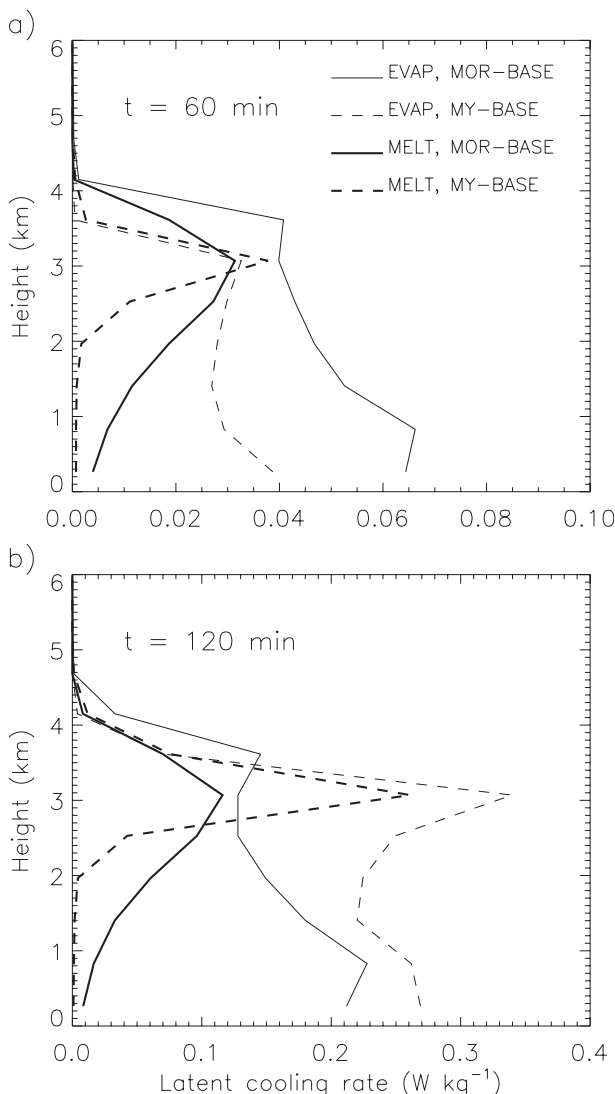
a)

b)

FIG. 9. Vertical profiles of latent cooling rates associated with melting (from cloud ice, snow, graupel, and hail) and rain evaporation for MOR-BASE (solid) and MY-BASE (dash) at time $t =$ (a) 60 and (b) 120 min.

TABLE 3. Domain-average, vertically integrated (surface to the height of the freezing level) latent cooling rates due to melting (from cloud ice, snow, graupel, and hail) and rain evaporation (W m^{-2}) at time $t = 60$ and 120 min, for selected runs.

Simulation	$t = 60$ min		$t = 120$ min	
	Melting	Evaporation	Melting	Evaporation
MOR-BASE	55.0	176.1	184.4	584.2
MOR-GRPL	23.6	93.1	139.3	606.3
MOR-DMR5	37.0	61.1	148.5	304.9
MY-BASE	24.8	93.4	169.9	810.8
MY-GRPL	23.2	94.2	169.3	757.8
MY-HAIL	48.3	150.3	220.0	745.2
MY-DMR5	47.4	122.2	204.8	619.6

runs diminish away from the surface, as illustrated by θ' at $z \sim 2.5$ km (Figs. 7c,d and 8c,d). At this level, the minimum values of θ' occur near the region of heaviest precipitation below the primary updraft cells in MOR-BASE and in the forward flank in MY-BASE, with relatively warm values in the rear flank in both simulations, indicating the relative shallowness of the cold pool in this region.

Diabatic cooling from both evaporation and melting contribute to the low-level cold pool (Fig. 9 and Table 3). Cooling associated with these processes is similar just below the freezing level, but the evaporative cooling rates are much larger throughout the rest of the melting layer (Fig. 9) and hence dominate the column-integrated cooling rates (Table 3). Note that the source of rain from melting has a larger impact on the column-integrated budget of rain mass compared to evaporation, but has much less impact on cooling rates because of the nearly order of magnitude difference in the enthalpy per mass of vaporization compared to melting. In both simulations, almost all of the frozen condensate melts before it reaches the surface, though melting occurs over a greater depth in MOR-BASE (Fig. 9). Column-integrated melting rates are larger in MOR-BASE (Table 3), indicating greater flux of frozen mass into the melting layer from above. These differences are reduced by $t = 120$ min. Evaporation rates are much larger in MOR-BASE earlier in the simulations (indicated by values at $t = 60$ min), but by $t = 120$ min MY-BASE has 39% larger column-integrated (surface to height of freezing level) evaporative cooling (Table 3). In general, these differences are consistent with the cold pool differences discussed above. Greater depth of the melting layer and larger melting and evaporation rates earlier in the simulation in MOR-BASE are consistent with fast-falling hail bringing precipitation rapidly toward the surface compared to the slower-falling graupel that dominates in MY-BASE (see section 4c).

MY-BASE has larger domain-averaged updraft and downdraft mass fluxes than MOR-BASE above $z \sim 2.5$ km

$t = 120$ min (Figs. 8a,b). The development of additional convective cells and heavier precipitation along the edge of the forward-flank downdraft in MY-BASE also contributes to the cooling in this region. These differences in low-level θ' are generally consistent with the differences in the dynamical structure between the simulations discussed above; namely, the stronger forward-flank downdraft and associated low-level convergence along its edge in MY-BASE (after $t = 60$ min), and stronger low-level convergence and upward motion along the rear flank of the primary right- and left-moving cells as well as the greater distance between these cells due to faster propagation of the cold pool edge in MOR-BASE. Differences in θ' between the
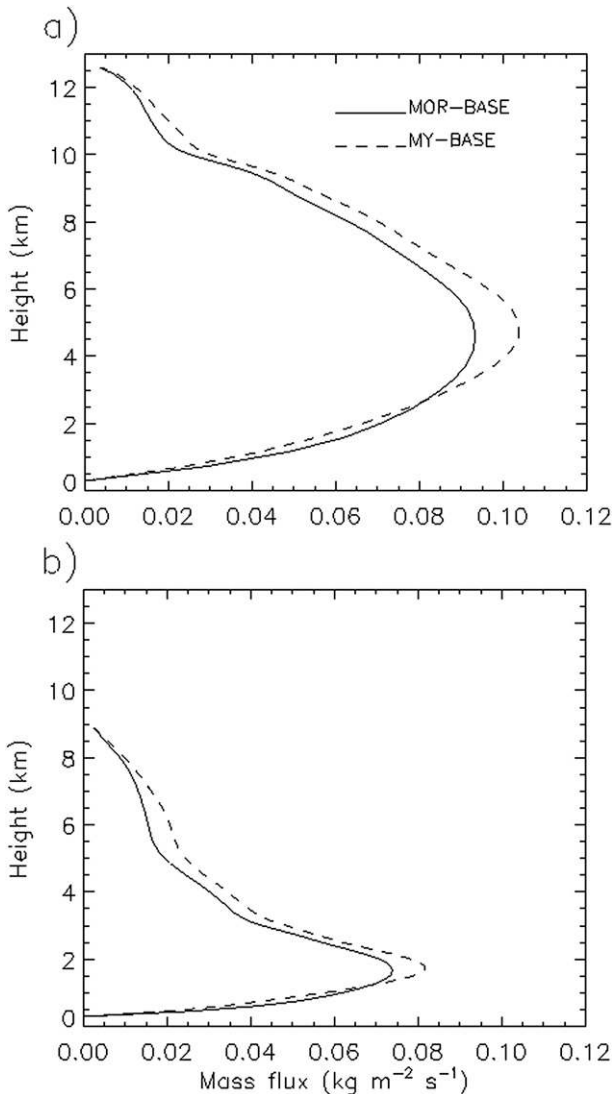
FIG. 10. Vertical profiles of domain-averaged (a) updraft mass flux and (b) downdraft mass flux for MOR-BASE (solid) and MY-BASE (dash) at time $t = 60$ min.

(Fig. 10), with the differences increasing after $t = 60$ min (not shown). MOR-BASE, on the other hand, has slightly larger vertical mass fluxes below 2.5 km. Stronger peak downdrafts in MOR-BASE are evident from the time series of peak downdraft velocity below 3.5 km (Fig. 11a). Stronger moist downdrafts in MOR-BASE are consistent with the greater latent cooling rates at low levels described above. Maximum updraft velocities are fairly steady and similar for the 2 runs after about $t = 60$ min, with values near 50 m s^{-1} (Fig. 11b). However, maximum updraft velocities are 5–10 m s^{-1} larger in MY-BASE between $t = 30$ and 50 min, which appears to be associated with differences in the simulations during and immediately following the storm splitting (see section 4a).

c. Surface precipitation and microphysics

Domain-averaged accumulated surface precipitation is approximately 3 times larger in MOR-BASE at $t = 60$ and 120 min (Table 2). Domain-averaged instantaneous precipitation rates are higher in MOR-BASE for the duration of the simulations, with the precipitation being predominately liquid. Domain-average profiles of the mass mixing ratios of the various hydrometeor species indicate near-surface rain mixing ratios are larger in MOR-BASE (Fig. 12). Larger rain mixing ratios in MOR-BASE are due in part to a larger flux of frozen condensate into the melting layer from above, as evidenced by the greater column-integrated melting rates (Table 3). Differences in low-level rain mixing ratios account for the larger surface precipitation rates in MOR-BASE, since the mean–mass raindrop fall speed near the surface is generally smaller, consistent with smaller mean–mass diameter, D_{mr}, compared to MY-BASE (Fig. 13). Differences in D_{mr} between the simulations are mainly due to different treatments of raindrop breakup and values of the maximum allowed mean drop size (size limiter), as detailed in section 5. Both larger rain mixing ratios and smaller mean drop sizes contribute to greater evaporation rates earlier in MOR-BASE (Fig. 9 and Table 3), and hence a stronger cold pool, since the evaporation rate is approximately proportional to $1/D_{mr}^2$ for a given mixing ratio. Differences in rain mixing ratio are reduced toward the end of the simulations and the column-integrated rain evaporation rate becomes larger in MY-BASE (Table 3).

Even though the flux of frozen condensate into the melting layer and hence column-integrated melting rates are larger in MOR-BASE than MY-BASE, especially earlier in the simulations, the domain-average graupel/hail mixing ratios are much larger in MY-BASE above the freezing level (Fig. 12). This apparent inconsistency is explained by the slower fallout of frozen hydrometeors in MY-BASE, which occurs as a result of two factors. First, graupel is the dominant rimed-ice specie in MY-BASE, with domain-mean hail mixing ratios <0.1% of the graupel mixing ratios above the freezing level. For a given mean particle size, graupel has a slower fall speed than hail, which is the prescribed rimed-ice type in MOR-BASE. Second, the mean–mass hail size in the region near the freezing level is generally much larger in MOR-BASE than the mean–mass size (combined graupel and hail) in MY-BASE (Fig. 14). Differences in graupel/hail mixing ratios between MOR-BASE and MY-BASE increase over the course of the simulations (Figs. 12a,b). By $t = 120$ min, the much larger graupel/hail mixing ratios in MY-BASE above the freezing level help to compensate for the slower fallout, and differences in the flux of frozen condensate into the melting layer between the runs are reduced. Note
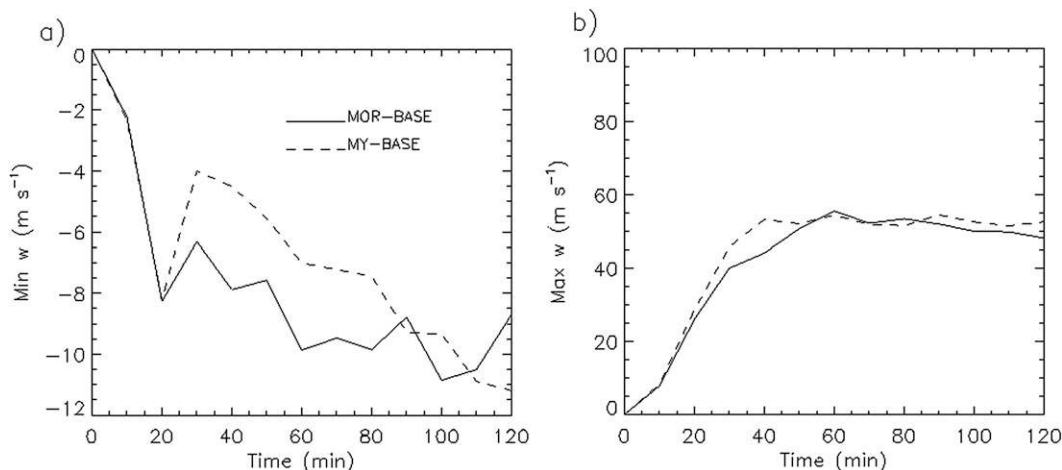
FIG. 11. Time evolution of (a) minimum vertical velocity (maximum downdraft) below 3.5 km and (b) maximum updraft velocity at all levels for MOR-BASE (solid) and MY-BASE (dash).

that domain-averaged snow mixing ratios in MY-BASE are nonzero but small (maximum values <0.01 g kg^{-1}). Although snow quantities at upper levels (~8–12 km) are much larger in MOR-BASE, snow does not contribute much mass to rain through melting since the mixing ratios near the melting level are small (Fig. 12). However, the tendency of MOR-BASE to retain more frozen condensate in the form of snow, with lower bulk fall velocities than graupel/hail, likely limits the flux of ice-phase hydrometeor mass into the melting layer from what it would be otherwise.

Differences in the net (domain integrated) condensation/deposition rate between the simulations explain some differences in the hydrometeor amounts. MY-BASE has a 10%–15% larger net condensation/deposition rate after about $t = 80$ min, consistent with the larger domain-averaged updraft mass flux above ~2.5 km compared to MOR-BASE, with smaller differences earlier in the simulations. However, this appears to be of secondary importance in explaining differences in hydrometeor quantities relative to the other factors described above, given that the hydrometeor mass in MY-BASE exceeds that of MOR-BASE by roughly a factor of 3 at $t = 120$ min.

5. Sensitivity tests

To elucidate some of the main causes of conspicuous differences in storm structure, precipitation, and cold pool characteristics between the two baseline simulations, a series of sensitivity experiments was performed. The main sensitivity tests are summarized in Table 1. The domain-averaged accumulated surface precipitation, minimum low-level θ', and fraction of domain area with a low-level cold pool for the various simulations at $t = 60$ and 120 min are listed in Table 2, with column-integrated domain-averaged evaporative cooling and melting rates for selected runs listed in Table 3.

a. Sensitivity to graupel/hail partitioning

A major difference between the MOR and MY schemes used in the baseline simulations is the treatment of graupel/hail. In this section, the sensitivity to the choice of graupel or hail is examined for runs with a single rimed-ice category (see Table 1). MOR-GRPL is identical to MOR-BASE except that the bulk density and V–D parameters of the rimed-ice category have been modified to correspond with those of medium-density graupel rather than high-density hail as in MOR-BASE (see Table 4). For the MY scheme, the graupel-only (MY-GRPL) and hail-only (MY-HAIL) runs are set up such that all initiation of all graupel and hail (i.e., from wet growth, collisional freezing, or probabilistic freezing of rain) is directed to the single rimed-ice category, with the appropriate density and V–D parameters. While the bulk densities of rain, graupel, and hail and V–D parameters for graupel are the same in MOR and MY, the V–D parameters for rain and hail differ (see Table 4). To allow a direct comparison of graupel-only and hail-only settings, additional sensitivity runs were performed with MOR, but using the rain and hail V–D parameters from MY. These tests are referred to as MOR-BASE-V and MOR-GRPL-V, using the hail and graupel settings for the rimed-ice category, respectively.

Plots of w and Z for MOR-GRPL and MY-HAIL at various heights and times are shown in Figs. 15–17. Results for MY-GRPL (not shown) are very similar to MY-BASE. The limited impact of including hail in MY-BASE is consistent with the very small domain-mean hail mixing ratios for this simulation described in section 4.
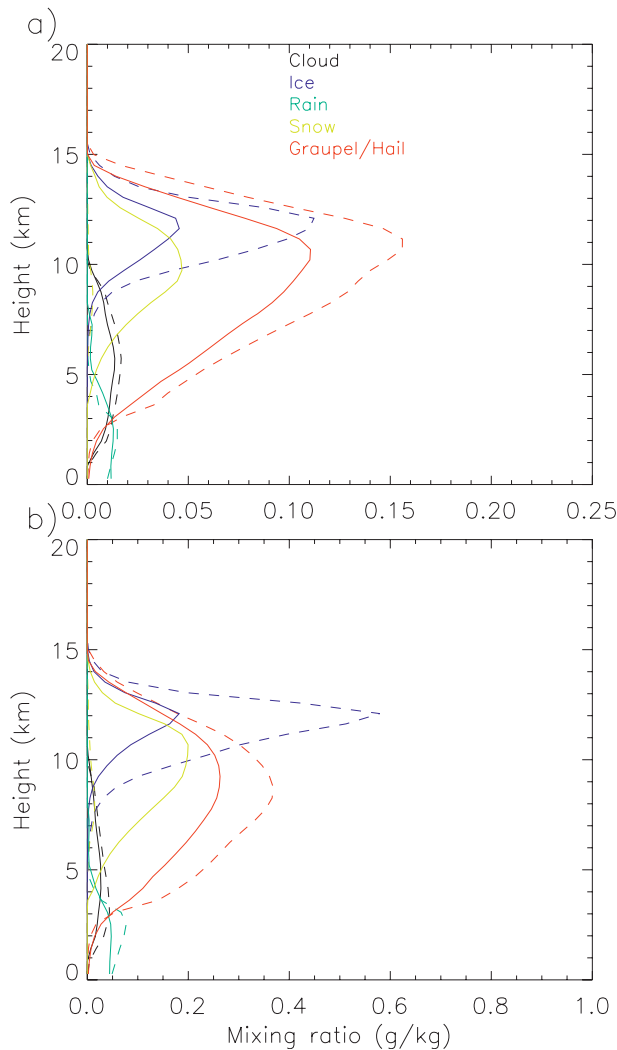
FIG. 12. Vertical profiles of horizontally averaged cloud droplet, cloud ice, rain, snow, and graupel/hail mixing ratios for MOR-BASE (solid) and MY-BASE (dash) at time $t =$ (a) 60 and (b) 120 min. Graupel and hail are summed for MY-BASE.

Many qualitative similarities are noted between the two hail-only simulations (MY-HAIL and MOR-BASE) and between the graupel-only simulations (and MY-BASE; Figs. 1–3 and 15–17). For example, MOR-GRPL produces a relatively long, narrow area of precipitation in the forward flank with large values of Z away from the primary updraft cores at midlevels (Fig. 16c), similar to MY-BASE (Fig. 2b) and MY-GRPL. MY-HAIL produces storm splitting that is nearly identical to MOR-BASE, with a low-level downdraft located between the left- and right-moving cells and relatively vigorous low-level updrafts aligned under the midlevel updrafts, as indicated by the w field at $t = 40$ min (cf. Figs. 15b and 1a). By $t = 120$ min, MY-HAIL also has strong low-level convergence and upward motion along the rear flank of the

left- and right-moving storm (Fig. 15f) similar to MOR-BASE (Fig. 1e), and with similar distance between the two primary cells ($\sim$70 km). Conversely, several storm features in MOR-GRPL and MY-GRPL are similar. There are also some notable differences, however, such as the much weaker forward-flank downdraft in MOR-GRPL and limited low-level convergence and secondary convection along its edge compared to MY-BASE (cf. Figs. 15e and 1f) and MY-GRPL.

A comparison of cold pool characteristics between the hail-only runs (MOR-BASE and MY-HAIL; Table 2) indicates that the cold pool strength and area are similar, though the area of $\theta' < -4$ K is larger in MOR-BASE (not shown). The cold pool is weaker for the graupel-only runs than the hail-only runs, particularly for MOR (see Table 2). The differences between MOR-GRPL and MOR-BASE are comparable to the difference in minimum θ' between MOR-BASE and MY-BASE. However, for MY the difference in minimum θ' between the graupel-only and hail-only runs is much smaller near the end of the simulation period (0.4 K at $t = 120$ min). The cold pool is stronger and larger in MY-GRPL than MOR-GRPL, especially in the forward-flank region by $t = 120$ min, which is consistent with the stronger forward-flank downdraft in MY-GRPL.

The choice of graupel or hail for a single rimed-ice category has a large impact on the mean–mass fall speed and hence residence time and lofting of frozen condensate. By $t = 120$ min, the midlevel ($z \sim$ 4–10 km) graupel mixing ratios are approximately 2–3 times larger in the graupel-only runs than the hail mixing ratios in the hail-only runs. Although there is more frozen condensate above the freezing level, there is a reduced flux of ice-phase mass into the melting layer as a result of the slower fall speed and hence lower cooling rate due to melting in the graupel-only runs, especially for MOR-GRPL (Table 3). These differences in melting also have important consequences for the low-level rain mixing ratios and evaporative cooling rates. In general, evaporative cooling rates are larger in the hail-only earlier in the simulations (as illustrated by results at $t = 60$ min), leading in part to the different cold pool characteristics discussed above. Note that evaporation rates are somewhat larger in the graupel-only compared to the hail-only runs later in the simulations for either MOR or MY, despite a smaller flux of ice into the melting layer as shown by the column-integrated melting rates at $t = 120$ min. This appears to result in part from smaller mean graupel size compared to hail, resulting in smaller mean raindrop size and hence greater evaporation rates. By the end of the simulations MOR-BASE and especially MOR-GRPL produce weaker evaporative cooling than either MY-HAIL or MY-BASE. This is consistent with the weaker cold pool in MOR-GRPL compared to
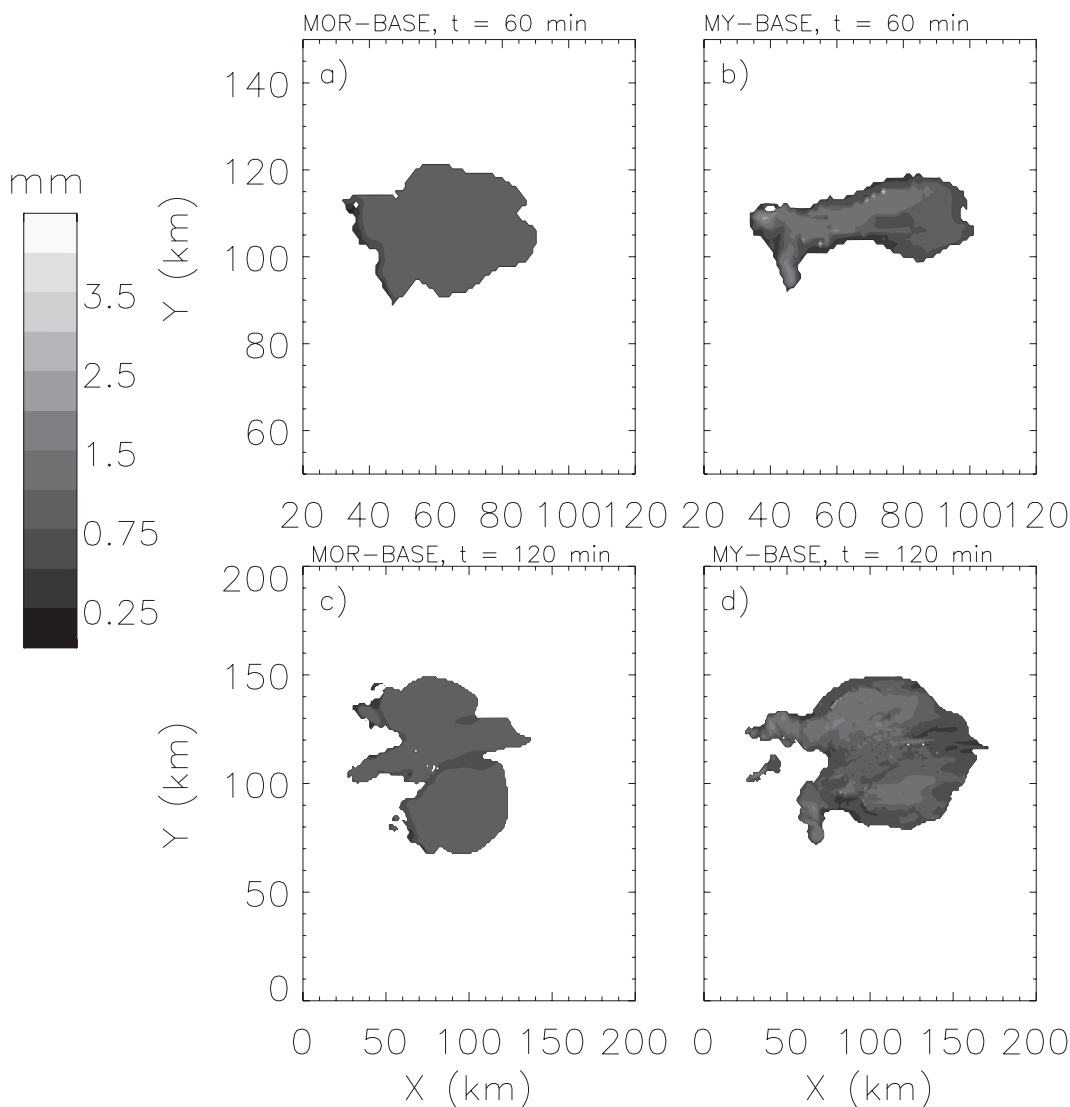
FIG. 13. Rain drop mean–mass diameter D_{mr} (shown only for locations with rain mixing ratio >0.01 g kg^{-1}) at height ~0.75 km for MOR-BASE at time t = (a) 60 and (c) 120 min, and MY-BASE at time t = (b) 60 and (d) 120 min.

MY-GRPL at t = 120 min, despite the smaller mean raindrop size in MOR-GRPL (not shown).

Differences in representation of the rimed-ice category as either hail or graupel also have important implications for the surface precipitation rate. MOR-GRPL and MY-GRPL produce very similar domain-averaged accumulated surface precipitation (Table 2). MOR-BASE and MY-HAIL also exhibit similar surface precipitation amounts, though MY-HAIL has slightly less (~25%) precipitation (Table 2). The larger surface precipitation rates in the hail-only runs are broadly consistent with the results of Gilmore et al. (2004) using a single rimed-ice category one-moment BMS, where N_0 and the bulk particle density were varied.

The MOR-BASE-V and MOR-GRPL-V simulations (using the MY V–D relations) are generally similar to MOR-BASE and MOR-GRPL in terms of storm structure and surface precipitation, indicating that differences between the MY and MOR fall velocity parameters for rain and hail have only a limited impact on overall structure. However, there are more important impacts on cold pool characteristics as seen in Table 2; namely, an approximately 2 K warmer minimum θ' in MOR-BASE-V compared to MOR-BASE, which likely explains some of the differences in cold pool strength between the baseline MOR and MY simulations. In general, the surface precipitation rate is less sensitive than the cold pool characteristics to hail and rain parameters, such as fall speed
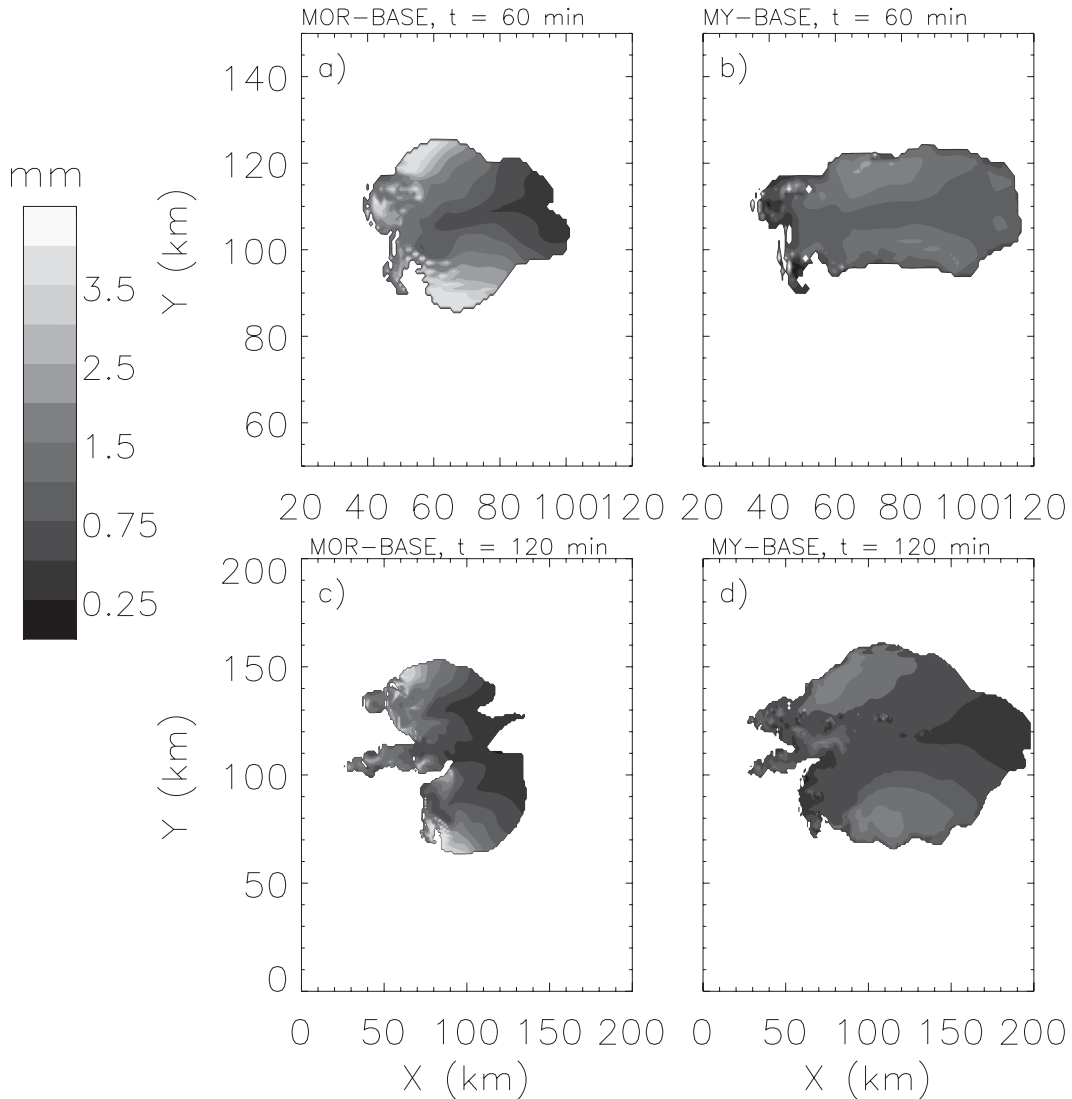
FIG. 14. As in Fig. 13, but for hail/graupel mean–mass diameter at a height of ~4.7 km. For MY-BASE, a combined hail/graupel mean diameter is obtained by mass weighting of the graupel and hail mean–mass diameters.

relations and, as described below, parameterization of drop breakup.

To investigate further the role of hail versus graupel parameter settings using a single rimed-ice category, two additional sensitivity tests were performed to isolate the impact of changes in either the *V–D* relation or bulk density using MOR. The MOR scheme was modified to use the *V–D* relation of hail and density of graupel in one run (MOR-HV), and *V–D* relation for graupel and density of hail in the other (MOR-GV). Qualitatively in terms of overall storm structure, these tests suggest that differences in the *V–D* relations, rather than bulk density, explain first-order differences between the graupel-only and hail-only simulations. In terms of surface precipitation

and cold pool characteristics, differences between MOR-HV and MOR-GV are fairly similar to differences between MOR-BASE and MOR-GRPL (i.e., the same sign, but somewhat reduced in magnitude; Table 2). However, the reduced magnitude of these differences suggests that the changes in bulk density do have a nonnegligible impact on the simulations.

b. Sensitivity to drop breakup

Another important difference between the baseline schemes is the treatment of raindrop breakup. The effects of this are examined by testing the two approaches used in the baseline schemes as well as two other drop breakup parameterizations in each scheme. Each of these methods

TABLE 4. Values of parameters in the MOR and MY simulations, unless otherwise stated (MKS units). V–D and m–D denote *velocity–diameter* and *mass–diameter*, respectively.

Symbol	Variable	MOR	MY
a_r	V–D coefficient for rain	842.0	149.1
a_i	V–D coefficient for ice	700.0	71.34
a_s	V–D coefficient for snow	11.72	11.72
a_g	V–D coefficient for graupel	19.3	19.3
a_h	V–D coefficient for hail	114.5	206.89
b_r	V–D exponent for rain	0.8	0.5
b_i	V–D exponent for ice	1.0	0.6635
b_s	V–D exponent for snow	0.41	0.41
b_g	V–D exponent for graupel	0.37	0.37
b_h	V–D exponent for hail	0.5	0.6384
c_c	m–D coefficient for cloud	$(\pi/6 \times \rho_w)$	$(\pi/6 \times \rho_w)$
c_r	m–D coefficient for rain	$(\pi/6 \times \rho_w)$	$(\pi/6 \times \rho_w)$
c_i	m–D coefficient for ice	$(\pi/6 \times \rho_i)$	$(\pi/6 \times \rho_i)$
c_s	m–D coefficient for snow	$(\pi/6 \times \rho_s)$	0.066
c_g	m–D coefficient for graupel	—	$(\pi/6 \times \rho_g)$
c_h	m–D coefficient for hail	$(\pi/6 \times \rho_h)$	$(\pi/6 \times \rho_h)$
d_c	m–D exponent for cloud	3	3
d_r	m–D exponent for rain	3	3
d_i	m–D exponent for ice	3	3
d_s	m–D exponent for snow	3	2
d_g	m–D exponent for graupel	—	3
d_h	m–D exponent for hail	3	3
ρ_w	Density of liquid water	1000 kg m^{-3}	1000 kg m^{-3}
ρ_i	Bulk density of ice	100 kg m^{-3}	1000 kg m^{-3}
ρ_s	Bulk density of snow	100 kg m^{-3}	*
ρ_g	Bulk density of graupel	400 kg m^{-3}	400 kg m^{-3}
ρ_h	Bulk density of hail	900 kg m^{-3}	900 kg m^{-3}
D_{mr_max}	Max D_m for rain	0.0009 m	0.005 m
D_{mr_shed}	D_m of rain for shed drops	0.001 m	0.001 m

* In MY, there is no fixed bulk density of snow; it implicitly varies with D as per the m–D parameters.

works implicitly, accounting for the effects of drop breakup by increasing the total number concentration of rain, N_r, when breakup is expected to occur, thereby reducing the mean–mass diameter, D_{mr}. The effects of the drop size limiter, where a maximum size for D_{mr} is imposed, is also relevant for the rain PSD and evaporation rates, and thus the sensitivity to the value of D_{mr_max}, is included in this discussion. To reduce the effects of other differences between the schemes, the hail-only runs with MY V–D parameters for rain and hail (MOR-BASE-V and MY-HAIL) are taken as the control simulations for this set of experiments.

In the baseline MOR scheme, there is no explicit parameterization of breakup and $D_{mr\_max} = 0.9$ mm is used for the drop size limiter (note that rain self-collection is included). The baseline MY scheme uses the collisional breakup parameterization from Ziegler (1985, hereafter Z85) [his Eq. (A17)] and sets $D_{mr\_max} = 5$ mm for the drop size limiter. In the Z85 breakup parameterization, the bulk collection efficiency, E_c, used in the rain self-collection equation, is reduced from the assumed value of

unity. This reduces the amount by which N_r decreases as a result of self-collection, thus it implicitly increases N_r as a result of collisional breakup. The other two parameterizations examined are similar but have different formulations for E_c (see below).

Five sets of experiments are conducted (see Table 1). In the first two sets, only the drop size limiter is active and there is no explicit parameterization of breakup. In the first experiment (MY-DMR0.9), D_{mr_max} is reduced from 5 to 0.9 mm in the MY control run (MY-HAIL), the value used in MOR-BASE. In the second set, the run MOR-DMR5 is performed, with D_{mr_max} increased in MOR-BASE-V from 0.9 to 5 mm, with a corresponding run MY-DMR5, with $D_{mr\_max} = 5$ mm in the MY scheme (as in MY-HAIL but with explicit breakup shut off). In the third experiment (MOR-BRK_Z), the Z85 breakup parameterization is implemented into MOR-BASE-V, as in MY-HAIL. In the fourth and fifth sets, the breakup parameterizations of Verlinde and Cotton [1993, hereafter VC93, their Eq. (A.22)] and Seifert [2008, hereafter S08, his Eq. (A13)] are used in both BMSs, with the corresponding runs referred to as MOR-BRK_VC, MY-BRK_VC, MOR-BRK_S, and MY-BRK_S. For all runs using the explicit breakup parameterizations (Z85; VC93' S08), $D_{mr\_max} = 5$ mm, whose large value minimizes the impact of the drop size limiter. As with Z85, the VC93 and S08 parameterizations implicitly represent collisional drop breakup by decreasing E_c for rain self-collection. Both the VC93 and S08 formulations represent breakup as a nudging of D_{mr} to an equilibrium value when it exceeds a given threshold. The values of E_c as a function of D_{mr} for Z85, VC93, and S08 are depicted in Fig. 18. S08 is the most active of the three breakup parameterizations, having the lowest E_c for a given D_m. Both the VC93 and S08 can have negative values of E_c implying that the combination of self-collection and breakup can in effect be a net source for N_r.

The overall storm structure and reflectivity fields are similar among the sensitivity runs examined in this section, with all of these simulations exhibiting features that are similar to those of the hail-only runs described above. Drop breakup also has a limited impact on the surface precipitation, with the domain-averaged accumulated amount at $t = 120$ min varying less than 24% between the runs for either MOR or MY (Table 2). The evolution of the minimum θ' from each simulation is shown in Fig. 19. Evaporation and hence cold pool strength are more sensitive to drop breakup using the MOR scheme. There is less sensitivity to the treatment of breakup in MY since other microphysical processes act to produce rain with lower D_{mr} than in MOR (see below), resulting in drop breakup being less active.

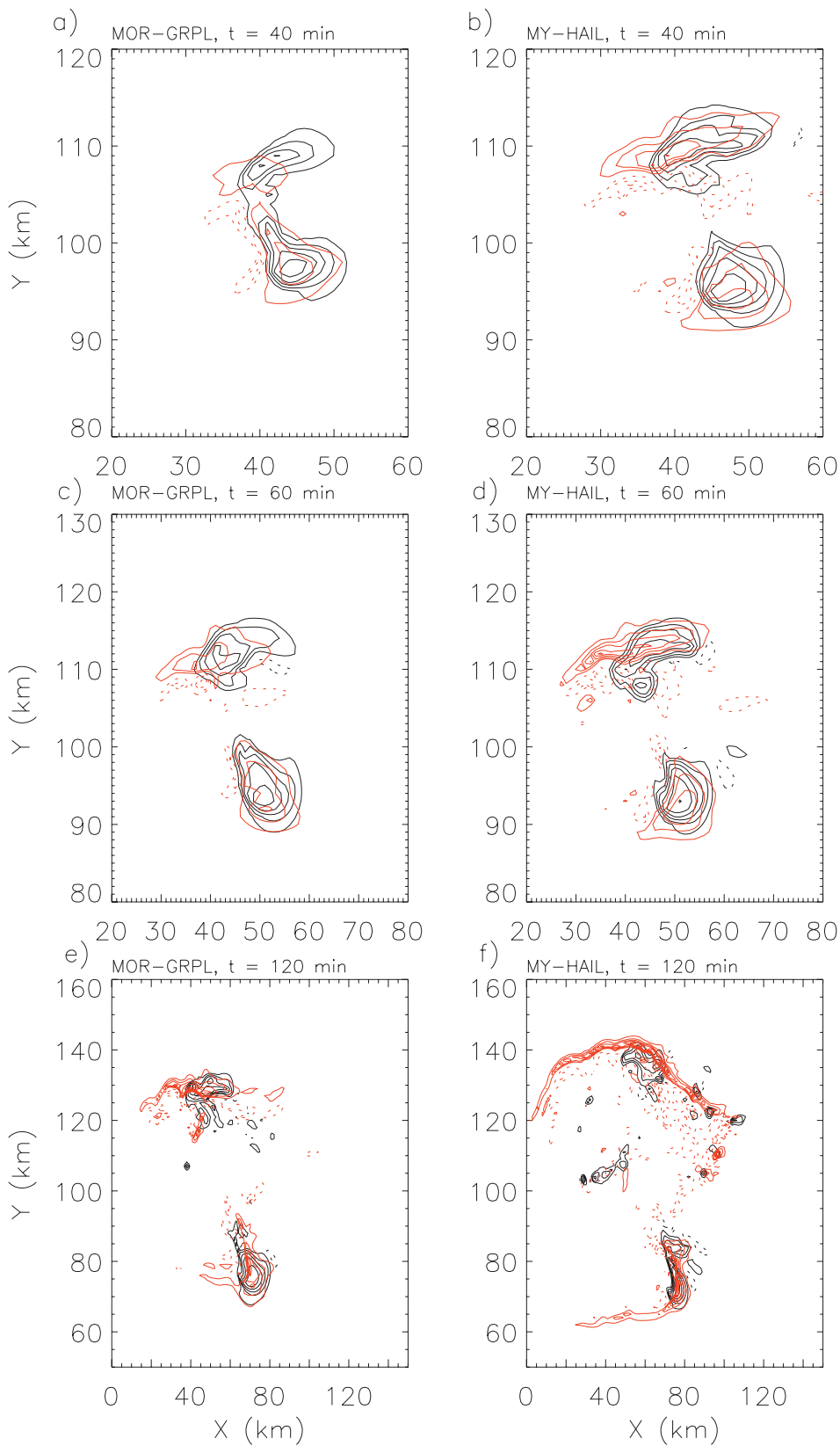Differences in the cold pool between MY and MOR are least when using S08, the most active breakup

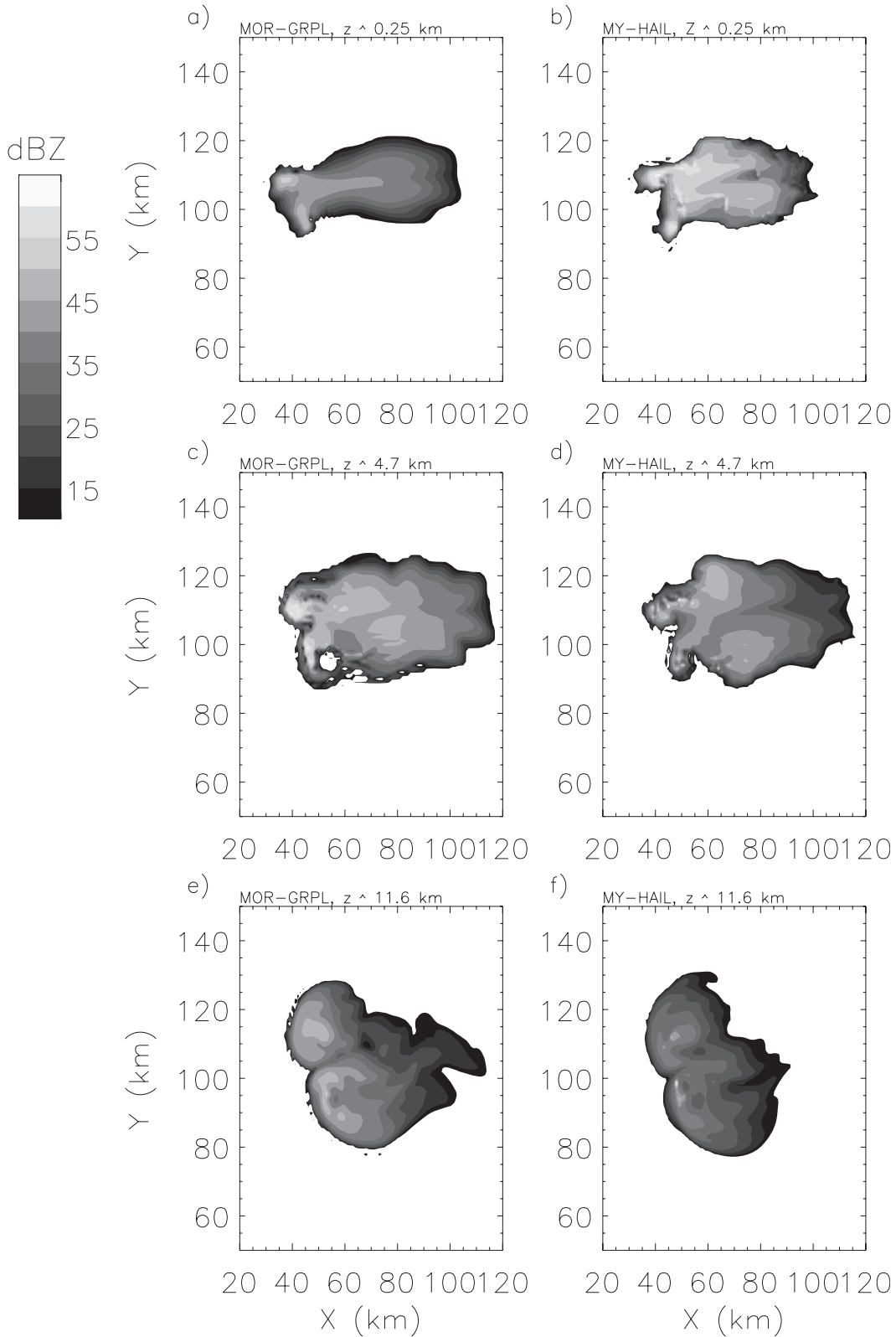FIG. 15. As in Fig. 1, but for the MOR-GRPL and MY-HAIL simulations.

FIG. 16. As in Fig. 2, but for the MOR-GRPL and MY-HAIL simulations at time $t = 60$ min.
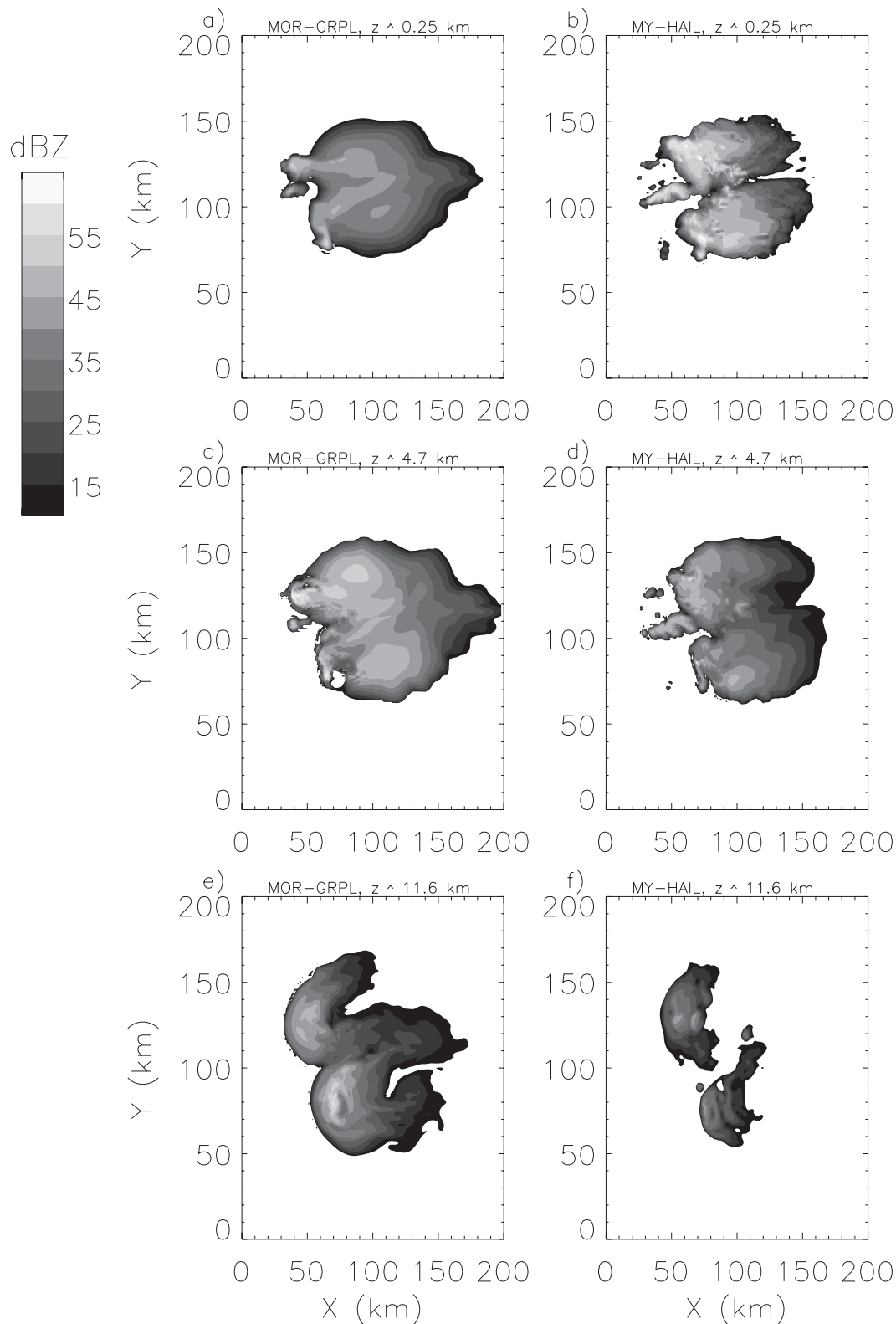
FIG. 17. As in Fig. 3, but for the MOR-GRPL and MY-HAIL simulations at time t = 120 min.
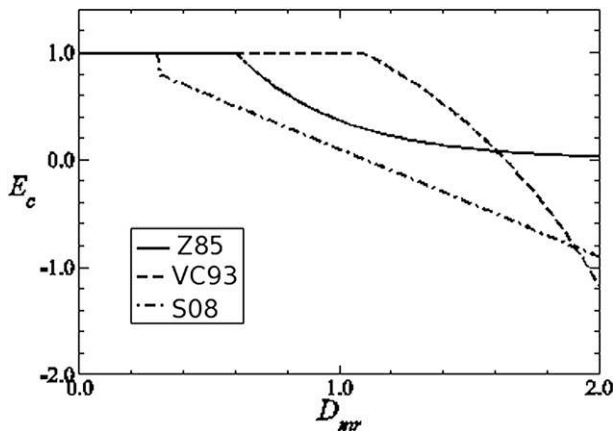
FIG. 18. Collection efficiencies E_c as a function of rain mass–mean diameter D_{mr} (mm) for the various drop breakup parameterizations.

parameterization (although differences in θ' and cold pool fraction are still rather large, see Table 2), as well as for runs with the low value of the drop size limiter ($D_{\mathrm{mr\_max}} = 0.9$ mm). In the simulations using the S08 breakup formulation or with limiter $D_{\mathrm{mr\_max}} = 0.9$ mm, the breakup and/or drop size limiter places a strong restriction on the drop sizes. With the less active breakup schemes (Z85; VC93) and with only a weakly restrictive drop size limiter ($D_{\mathrm{mr\_max}} = 5$ mm), drop breakup plays a more limited role, and hence the larger differences in the simulations are due the treatment of other processes in the MY and MOR schemes. This is illustrated by the 6.4 K warmer minimum θ' at $t = 120$ min in MOR-DMR5 than MY-DMR5 (Fig. 19 and Table 2). With both the Z85 and VC93 parameterizations, the minimum θ' is 3.6–3.9 K warmer using MOR than MY at $t = 120$ min. There are also large differences between MOR and MY in cold pool extent in these runs.

There does not appear to be any single factor leading to the much weaker cold pool in MOR compared to MY in runs using the less aggressive breakup schemes (e.g., MOR-DMR5 and MY-DMR5). However, analysis indicates that some of the differences in θ' can be attributed to differences in the snow and hail fields near the freezing level. Even though all of these runs use a single rimed-ice category with hail settings, MOR has much larger mean hail sizes than MY at $z \sim 4.7$ km (Fig. 20). These differences help produce much larger mean drop size in MOR-DMR5 upon melting (Fig. 21), and hence a reduced evaporative cooling rate (Table 3) and weaker cold pool (Table 2). There is also a smaller mass of frozen condensate near the freezing level in MOR-DMR5 (not shown), leading to a reduced flux of ice into the melting layer, lower column-integrated melting rates (Table 3), and smaller domain-mean rain mixing ratio compared to MY-DMR5.
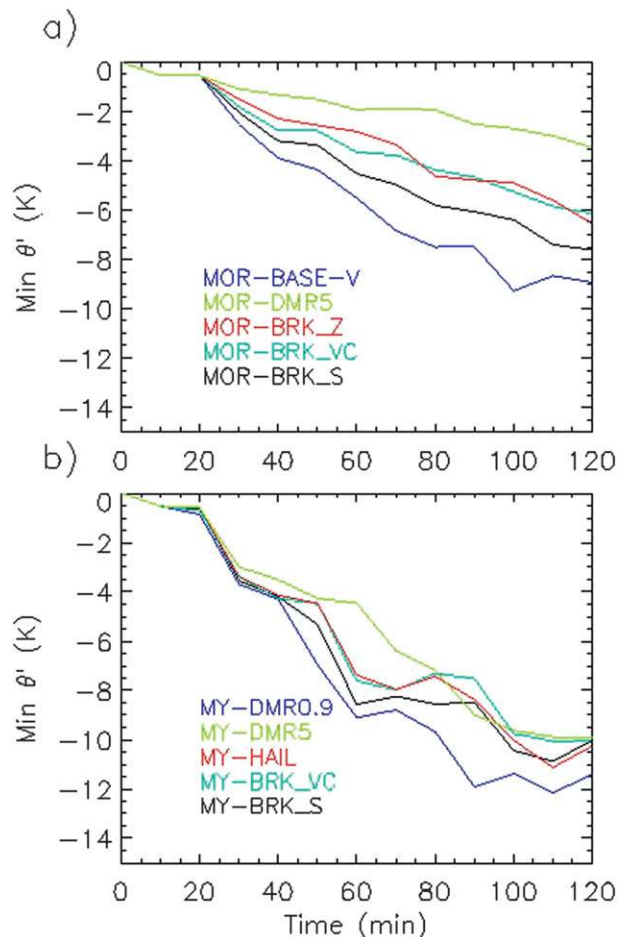

FIG. 19. Time evolution of low-level ($z \sim 0.25$ km) minimum θ' for the various drop breakup sensitivity simulations for (a) MOR and (b) MY.

To investigate further the impact of hail size on rain through melting, additional sensitivity tests were conducted, similar to MOR-DMR5 and MY-DMR5, but with melting assumed to produce rain with a $D_{\mathrm{mr}} = 1$ mm, regardless of hail size. This is different from the baseline schemes that conserve number concentration of graupel/hail during melting. The change results in smaller differences in cold pool characteristics between MOR and MY. For example, differences in minimum θ' are 2 K less than the differences between MOR-DMR5 and MY-DMR5 at $t = 120$ min. Another factor contributing to the warmer cold pool in MOR-DMR5 is autoconversion of cloud to rain. Cloud water is more widespread and has larger mass contents in MY-DMR5 than MOR-DMR5, leading to greater production of small rain drops through autoconversion and hence smaller mean drop size. Sensitivity tests using MOR-DMR5 and MY-DMR5, but with autoconversion shut off, exhibit differences in minimum θ'
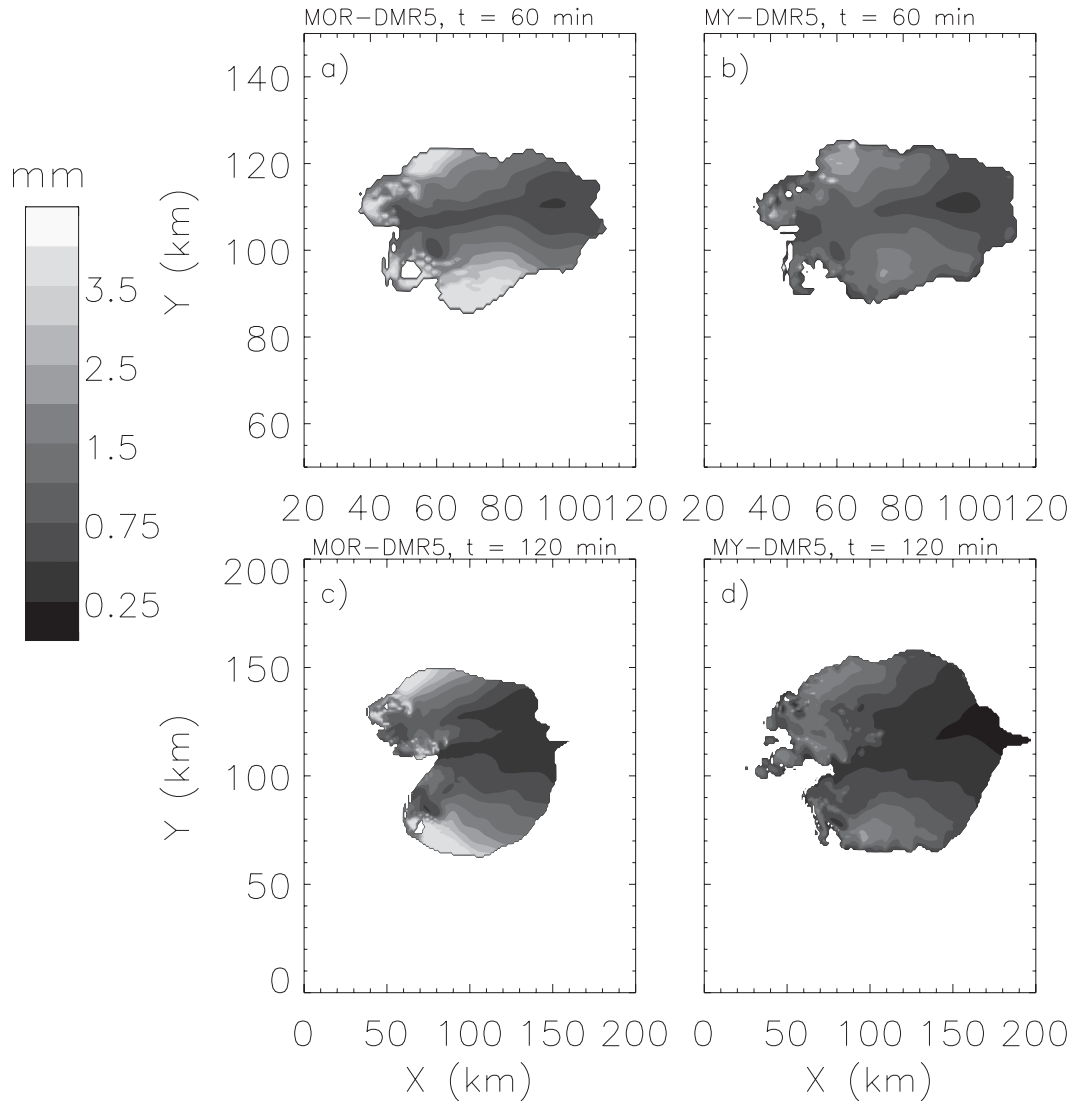
FIG. 20. As in Fig. 15, but for hail mean–mass diameter at a height of ~4.7 km for the MOR-DMR5 and MY-DMR5 simulations.

that are 3.1 K less than the differences between MOR-DMR5 and MY-DMR5 at $t = 120$ min.

6. Summary and conclusions

Simulations of an idealized supercell were conducted using the WRF model with the MOR and MY two-moment bulk microphysics schemes. Despite the overall similar approaches of the parameterizations, the simulations using the baseline versions of the schemes were distinctly different in terms of storm dynamics, reflectivity structure, surface precipitation, and cold pool strength and extent. A series of sensitivity experiments was conducted to identify the specific causes for the main differences in the baseline simulations, with the focus on the treatment

of graupel/hail, specifically the number of categories and the assumed single-category type, and the parameterization of raindrop breakup. Differences in these aspects of the two schemes were found to be crucial in explaining the conspicuous differences between the baseline runs.

Graupel-only simulations with each scheme were similar to each other but notably different from the hail-only simulations (which were also similar to one another), in terms of storm structure, surface precipitation rate, and cold pools. There were some notable exceptions, such as the much stronger forward-flank downdraft and stronger cold pool near the end of the simulations in MY compared to MOR for the graupel-only runs. Although graupel and hail are separate categories in the baseline MY scheme, inclusion of hail appeared to have relatively little impact
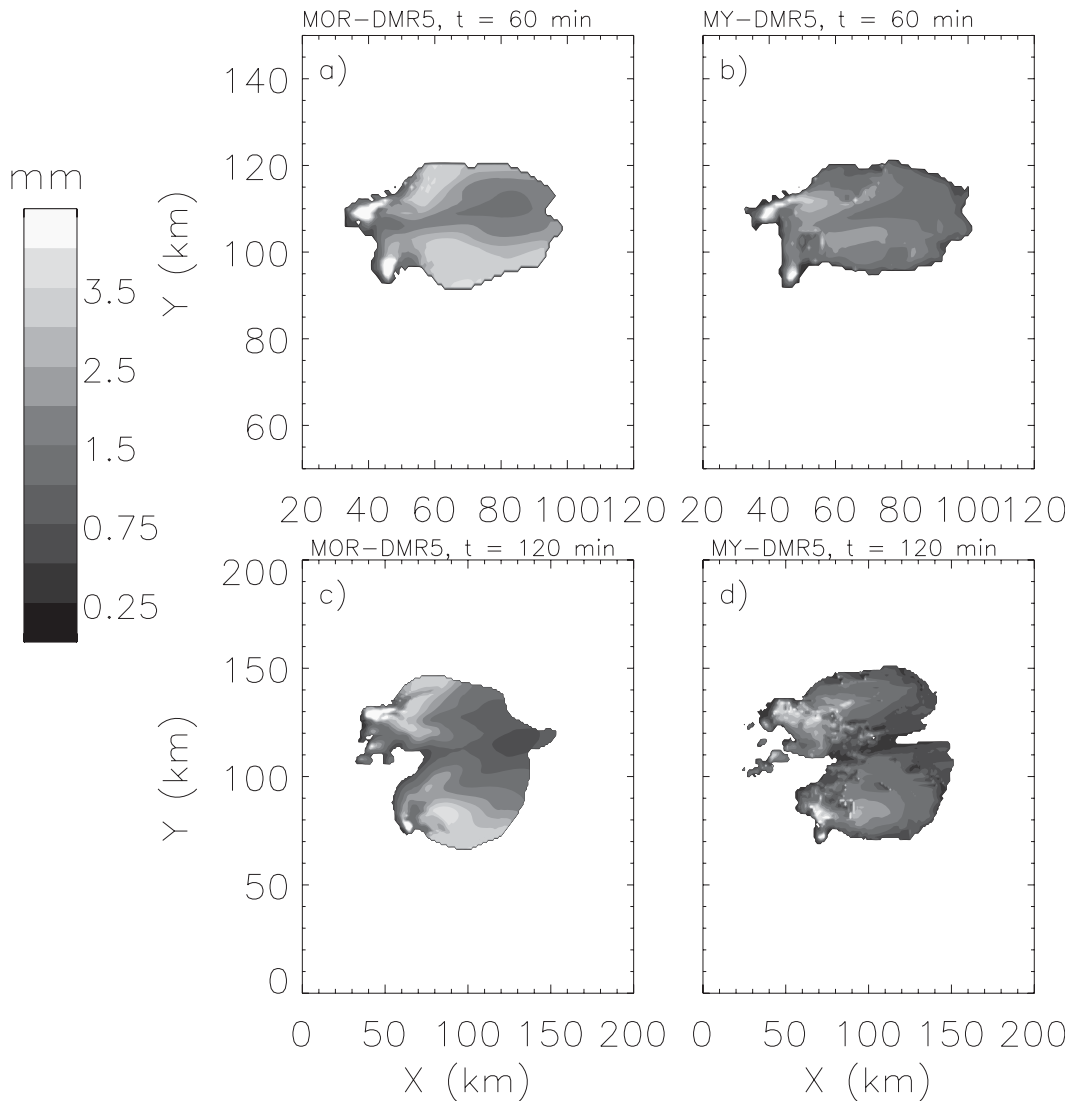
FIG. 21. As in Fig. 13, but for rain mean–mass diameter at a height of ~0.75 km for the MOR-DMR5 and MY-DMR5 simulations.

on the simulation and the two-category baseline MY run was very similar to the graupel-only MY run, highlighting uncertainties in hail particle initiation. This study illustrates the high degree of sensitivity of supercell simulations to the assumptions made about the type of rimed ice when represented by a single category in two-moment bulk schemes. Tests also suggest that some differences in cold pool strength between the baseline runs were due to the use of different fall speed parameters for rain and hail between the schemes.

The characteristics of the cold pool were highly sensitive to the parameterization of raindrop breakup for the MOR scheme. In contrast, other microphysical processes in the MY scheme produced relatively small rain sizes and thus the choice of drop breakup parameterization had much

less of an impact. For simulations with the same breakup formulation, fall speed parameters, and settings for hail as the single rimed-ice specie, MOR produced larger mean–mass rain diameters and a much weaker cold pool than MY when using the less aggressive breakup parameterizations. Thus, the use of a small value (0.9 mm) for the drop size limiter in the baseline MOR scheme, compared to less stringent limiter (5 mm) in the baseline MY scheme, helped to compensate for other differences that were revealed when using the less aggressive breakup schemes. Although no single factor was identified that could account for these other differences, sensitivity tests indicate that smaller mean hail particle size near the freezing level and more autoconversion in MY contributed to the relatively small raindrop size and stronger cold pool

in these runs. In terms of surface precipitation, the treatment of breakup had little impact for either scheme.

The microphysical processes that are parameterized in the type of BMSs examined here are numerous, complex, and interact in a highly nonlinear fashion. While this study highlights important elements in the MOR and MY schemes that led to the major differences between the baseline simulations, further investigation is needed to understand the role of other contributing factors. Future investigation on the treatment of graupel and hail will include a detailed examination of hail initiation and further study of the sensitivity to the number and type of rimed-ice categories for different types of convective systems. We emphasize that while the sensitivity to the treatment of graupel/hail and drop breakup has been investigated, specific recommendations for parameter settings cannot be made based on idealized case studies, but rather a close comparison of real-case simulations to observations is required.

While two-moment BMSs have been shown to improve aspects of storm simulations relative to using one-moment schemes, the large differences in results produced by MOR and MY highlight uncertainties associated with two-moment schemes in general. As modelers move away from the use of one-moment bulk schemes and add more degrees of freedom in the representation of cloud microphysical processes, they must be cognizant of such uncertainties and take care not to assume that simulations using multimoment parameterizations will converge simply due to the added complexity. These results also highlight the critical need for further observational studies of PSDs and ice particle properties, such as density and fall velocities, to appropriately specify parameter settings in the microphysics schemes.

APPENDIX

Description of the Microphysics Schemes

a. MOR microphysics scheme

The MOR scheme is based on the parameterization described in Morrison et al. (2005) and subsequently implemented into the fifth-generation Pennsylvania State University–National Center for Atmospheric Research (PSU–NCAR) Mesoscale Model (MM5; Morrison and Pinto 2005, 2006; Morrison et al. 2008) and WRF (MTT09; Solomon et al. 2009). For a complete description, interested readers are referred to Morrison et al. (2005) and MTT09 and references therein. A brief overview of the scheme is provided here to facilitate discussion of results, with emphasis on the aspects examined in the sensitivity tests.

The WRF-release version of the scheme predicts the mass mixing ratio q_x for each $x = c, i, s, r, g$, corresponding to five hydrometeor categories: *cloud* (liquid droplets), *ice* (pristine crystals), *snow* (large crystals/aggregates), *rain* (precipitating drops), and *graupel/hail* (either lump graupel *or* hail, depending on the parameter settings, as described below), respectively. It also predicts the total number concentration N_x for $x = i, s, r, g$. The PSD for each hydrometeor category x are represented by a complete gamma function of the form:

$$N_x(D) = N_{0x} D^{\mu_x} e^{-\lambda_x D}, \qquad (A1)$$

where N_{0x}, λ_x, and μ_x are the intercept, slope, and shape parameters, respectively, and D is the particle diameter. The parameters N_{0x} and λ_x can be computed from the prognostic variables, q_x and N_x, assuming a specified value of μ_x, by

$$\lambda_x = \left[\frac{c_x N_x \Gamma(\mu_x + 4)}{q_x \Gamma(\mu_x + 1)} \right]^{1/d_x} \qquad (A2)$$

and

$$N_{0x} = \frac{N_x \lambda_x^{\mu_x + 1}}{\Gamma(\mu_x + 1)}, \qquad (A3)$$

where Γ is the Euler gamma function and the parameters c_x and d_x are parameters for the assumed power-law mass–diameter (m–D) relationship:

$$m_x(D) = c_x D^{d_x}. \qquad (A4)$$

All particles are assumed to be spherical with constant bulk densities ρ_x. Thus, for each category $c_x = (\pi/6 \times \rho_x)$ and $d_x = 3$. For cloud droplets, μ_c is a function of the predicted value of N_c, based on observations (see MTT09), and varies from 2 to 10. All other categories have $\mu_x = 0$ and hence have inverse-exponential PSDs. The moment-weighted bulk fall velocities for each of the prognostic moments are computed using an assumed power-law velocity–diameter (V–D) relation:

$$V_x(D) = \gamma a_x D^{b_x}, \qquad (A5)$$

where $\gamma = (\rho_0/\rho)^{0.54}$ is the air density correction factor; with ρ and ρ_0 equal to the air density aloft and near the surface, respectively; and a_x and b_x are empirically determined parameters, appropriately chosen for the hydrometeor type. The values for the bulk densities and fall velocity parameters for the MOR scheme are summarized in Table 4. Numerically, sedimentation of hydrometeor mass mixing ratio and total number concentration is calculated using a first-order forward-in-time backward-in-space Eulerian advection scheme, which is substepped as necessary based on the Courant stability criterion.

Heavily rimed ice is represented by a single category, where the m–D and V–D parameters are characteristic of either medium-density graupel or high-density hail. The parameters for the rimed-ice category in the baseline simulation are set for hail (Table 4), which has been used for previous simulations of continental deep convection using the scheme (e.g., James and Markowski 2010; Luo et al. 2010). For some of the sensitivity tests discussed in section 5, the parameters are set for lump graupel[A1] and the rimed-ice category is referred to as graupel.

The parameterization of the processes of autoconversion of cloud water to form rain and accretion of cloud by rain are given by Khairoutdinov and Kogan (2000). The cloud droplet concentration, N_c, which is important in determining the autoconversion rate, is specified to be constant at 250 cm^{-3} for this study, which is the default value in the WRF release version of the scheme and appropriate for a relatively clean continental air mass. There is some sensitivity to increasing droplet concentration (e.g., weakening of cold pools), but detailed discussion of this issue is beyond the scope of this paper. The bulk effects of raindrop breakup for the WRF v3.1 release of the MOR scheme are treated purely implicitly by limiting rain drop mean–mass (or mean–volume) diameter, D_{mr}, given by

$$D_{\mathrm{mr}} = \left(\frac{6\rho q_r}{\pi \rho_w N_r}\right)^{1/3}, \qquad (A6)$$

with a maximum allowable value of $D_{\mathrm{mr\_max}} = 0.9$ mm.[A2] This limit is imposed by increasing N_r whenever D_{mr} exceeds this maximum value, $D_{\mathrm{mr\_max}}$, such that the resulting D_{mr} is exactly equal to $D_{\mathrm{mr\_max}}$. In addition to implicitly accounting for breakup, this drop size limiter is

necessary to prevent unrealistically large mean particle sizes that can result artificially from differential sedimentation (i.e., uncontrolled size sorting) in two-moment schemes (MY05a).

Ice crystals are initiated from primary nucleation, rimesplintering, and homogeneous freezing of cloud droplets. Conversion of ice to snow is based on diffusional growth of ice to a size above a threshold of 125 μm, following Harrington et al. (1995). Graupel (or hail) forms because of conversion from snow due to riming and from probabilistic and collisional freezing of rain. The melting of snow and graupel or hail is parameterized by a diffusional heat balance and assumes, as the closure assumption for the N tendency, that D_m is constant during melting. The total particle number concentration is assumed to be conserved; that is, the increase in N_r due to melting equals the decrease in the number concentration of the melting ice-phase category. Cloud ice is assumed to melt instantly to rain when the ambient air temperature is greater than 0°C. Shedding of liquid water during wet growth of graupel/hail is assumed to produce rain with $D_{\mathrm{mr}} = 1$ mm for the shed drops, though the size of raindrops is ultimately limited to $D_{\mathrm{mr\_max}}$ (0.9 mm in the baseline configuration) by the drop size limiter.

The radar reflectivity is computed following Ferrier (1994). No modification is made to account for increased reflectivity for partially melted ice-phase categories in this study.

b. MY microphysics scheme

The MY scheme is based on (MY05a,b) and references therein, with modifications described in Milbrandt et al. (2008) and Milbrandt et al. (2009). The full version is a three-moment BMS with prognostic equations for q_x, N_x, and the radar reflectivity Z_x for $x = c, r, i, s, g, h$ corresponding to the six hydrometeor categories: *cloud* (liquid droplets), *rain* (precipitating drops), *ice* (pristine crystals), *snow* (large crystals/aggregates), *graupel* (medium-density rimed ice), and *hail* (high density rimed ice and/or frozen drops). The DSD of each category is represented by (A1). The two-moment version, with prognostic equations for q_x and N_x only, has options for either fixed μ_x or for variable μ_x, determined by a diagnostic function of D_{mx}, for the precipitating categories (all except cloud). For direct comparison with MOR, only the two-moment fixed-μ_x version of MY, which has recently been implemented into the WRF model,[A3] is used in this study. For consistency with MOR, we have

---

[A1] For the official release of WRF, the default MOR scheme has parameter settings for the rimed-ice category corresponding to medium-density lump graupel, with a switch in the code to modify these settings to represent high-density hail.

[A2] For official release of WRF v3.2, raindrop breakup in the default MOR scheme is treated using a modified version of the parameterization of Verlinde and Cotton (1993), with $D_{\mathrm{mr\_max}} = 5$ mm.

[A3] For official release of v3.1 of WRF, only the MOR scheme is available. The MY scheme is available as a microphysics scheme option in the public release of v3.2.

set $\mu_x = 0$ for $x = i, r, s, g, h$, which is the default configuration for the WRF release. For cloud droplets, $\mu_x = 3$. The $m–D$ and $V–D$ parameters for the various species are listed in Table 4. The bulk densities for rain, graupel, and hail and fall speed parameters for snow and graupel are identical to those in MOR, but there are differences in fall speed parameters for rain and hail. Aspects of MY that differ notably from MOR or that pertain to the following analysis and discussion are summarized below.

The cloud droplet nucleation and warm-rain coalescence components of the MY scheme are based on Cohard and Pinty (2000), with the autoconversion parameterization from Berry and Reinhardt (1974). For all of the simulations discussed here, a constant droplet concentration of $N_c = 250$ cm^{-3} is prescribed, as in MOR. Raindrop breakup is parameterized following Ziegler (1985) and Cohard and Pinty (2000), which acts by reducing the bulk collection efficiency for rain self-collection. A drop size limiter also applied, similar to the MOR scheme, but for $D_{mr\_max} = 5$ mm.

Ice initiation is based on primary nucleation, rime splintering, and homogeneous freezing. Conversion of ice to snow is based on the diffusional growth of an ice crystal to the size of an embryo snow crystal diameter of 125 μm. Snow is converted to graupel when the riming rate exceeds the diffusional growth rate by a factor of 3. The MY scheme has two distinct categories of rimed ice (graupel and hail). Graupel is converted to hail when it undergoes wet growth. Hail can also be initiated from probabilistic and collisional freezing of rain. Shedding during wet growth of hail is treated in the same way as the wet growth of graupel/hail in the MOR scheme, where excess water is shed to rain with an assumed $D_{mr} = 1$ mm for shed drops. Melting of the ice-phase categories is treated the same as MOR. Numerically, sedimentation of mass mixing ratio and number concentration is computed using a box-Lagrangian advection scheme following Kato (1995). This method is the same as the first-order scheme used in MOR when the sedimentation Courant number is less than unity, which is the case for all locations and times given the time step and vertical grid spacing used in these simulations. The radar reflectivity is computed in the same way as for the MOR scheme.

REFERENCES

Berry, E., and R. Reinhardt, 1974: An analysis of cloud drop growth by collection. Part II: Single initial distributions. *J. Atmos. Sci.,* **31,** 1825–1831.

Cohard, J.-M., and J.-P. Pinty, 2000: A comprehensive two-moment warm microphysical bulk scheme. I: Description and tests. *Quart. J. Roy. Meteor. Soc.,* **126,** 1815–1842.

Cohen, C., and E. W. McCaul Jr., 2006: The sensitivity of simulated convective storms to variations in prescribed single-moment microphysics parameters that describe particle distributions, sizes, and numbers. *Mon. Wea. Rev.,* **134,** 2547–2565.

Cotton, W. R., G. J. Tripoli, R. M. Rauber, and E. A. Mulvhill, 1986: Numerical simulations of the effects of varying ice crystal nucleation rates and aggregation processes on orographic snowfall. *J. Climate Appl. Meteor.,* **25,** 1658–1680.

Dawson, D. T., II, M. Xue, J. A. Milbrandt, and M. K. Yau, 2010: Comparison of evaporation and cold pool development between single-moment and multimoment bulk microphysics schemes in idealized simulations of tornadic thunderstorms. *Mon. Wea. Rev.,* **138,** 1152–1171.

Ferrier, B. S., 1994: A double-moment multiple-phase four-class bulk ice scheme. Part I: Description. *J. Atmos. Sci.,* **51,** 249–280.

——, W.-K. Tao, and J. Simpson, 1995: A double-moment multiple-phase four-class bulk ice scheme. Part II: Simulations of convective storms in different large-scale environments and comparisons with other bulk parameterizations. *J. Atmos. Sci.,* **52,** 1001–1033.

Fovell, R. G., and Y. Ogura, 1988: Numerical simulation of a midlatitude squall line in two dimensions. *J. Atmos. Sci.,* **45,** 3846–3879.

Gilmore, M. S., and L. J. Wicker, 1998: The influence of midtropospheric dryness on supercell morphology and evolution. *Mon. Wea. Rev.,* **126,** 943–958.

——, J. M. Straka, and E. N. Rasmussen, 2004: Precipitation uncertainty due to variations in precipitation particle parameters within a simple microphysics scheme. *Mon. Wea. Rev.,* **132,** 2610–2627.

Harrington, J. Y., M. P. Meyers, R. L. Walko, and W. R. Cotton, 1995: Parameterization of ice crystal conversion processes due to vapor deposition for mesoscale models using double-moment basis functions. Part I: Basic formulation and parcel model results. *J. Atmos. Sci.,* **52,** 4344–4366.

James, R. P., and P. M. Markowski, 2010: A numerical investigation of the effects of dry air aloft on deep convection. *Mon. Wea. Rev.,* **138,** 140–161.

Kain, J. S., and Coauthors, 2008: Some practical considerations regarding horizontal resolution in the first generation of operational convection-allowing NWP. *Wea. Forecasting,* **23,** 931–952.

Kato, T., 1995: A box-Lagrangian rain-drop scheme. *J. Meteor. Soc. Japan,* **73,** 241–245.

Kessler, E., 1969: *On the Distribution and Continuity of Water Substance in Atmospheric Circulations. Meteor. Monogr.,* No. 32, Amer. Meteor. Soc., 84 pp.

Khain, A., A. Pokrovsky, M. Pinsky, A. Seifert, and V. Phillips, 2004: Simulation of effects of atmospheric aerosols on deep turbulent convective clouds using a spectral microphysics mixed-phase cumulus cloud model. Part I: Model description and possible application. *J. Atmos. Sci.,* **61,** 2963–2982.

Khairoutdinov, M. F., and Y. Kogan, 2000: A new cloud physics parameterization in a large-eddy simulation model of marine stratocumulus. *Mon. Wea. Rev.,* **128,** 229–243.

Koenig, L. R., and F. W. Murray, 1976: Ice-bearing cumulus cloud evolution: Numerical simulation and general comparison against observations. *J. Appl. Meteor.,* **15,** 747–762.

Kong, F., and M. K. Yau, 1997: An explicit approach to microphysics in the MC2. *Atmos.–Ocean,* **35,** 257–291.

Lean, H. W., P. A. Clark, M. Dixon, N. M. Roberts, A. Fitch, R. Forbes, and C. Halliwell, 2008: Characteristics of high-resolution versions of the Met Office Unified Model for forecasting convection over the United Kingdom. *Mon. Wea. Rev.,* **136,** 3408–3424.

Lin, Y.-L., R. D. Farley, and H. D. Orville, 1983: Bulk parameterization of the snow field in a cloud model. *J. Climate Appl. Meteor.,* **22,** 1065–1092.

Luo, Y., Y. Wang, H. Wang, Y. Zheng, and H. Morrison, 2010: Modeling convective-stratiform precipitation processes on a Meiyu front with the WRF model: Comparison with observations and sensitivity to cloud microphysics parameterizations. *J. Geophys. Res.,* **115,** D18117, doi:10.1029/2010JD013873.

Mansell, E. R., 2008: EnKF analysis and forecast predictability of a tornadic supercell storm. Preprints, *24th Conf. on Severe Local Storms,* Savannah, GA, Amer. Meteor. Soc., P5.2. [Available online at http://ams.confex.com/ams/24SLS/techprogram/paper_142059.htm.]

McCumber, M., W.-K. Tao, J. Simpson, R. Penc, and S.-T. Soong, 1991: Comparison of ice-phase microphysical parameterization schemes using numerical simulations of tropical convection. *J. Appl. Meteor.,* **30,** 985–1004.

Meyers, M. P., R. L. Walko, J. Y. Harrington, and W. R. Cotton, 1997: New RAMS cloud microphysics. Part II: The two-moment scheme. *Atmos. Res.,* **45,** 3–39.

Milbrandt, J. A., and M. K. Yau, 2005a: A multimoment bulk microphysics parameterization. Part I: Analysis of the role of the spectral shape parameter. *J. Atmos. Sci.,* **62,** 3051–3064.

——, and ——, 2005b: A multimoment bulk microphysics parameterization. Part II: A proposed three-moment closure and scheme description. *J. Atmos. Sci.,* **62,** 3065–3081.

——, and ——, 2006: A multimoment bulk microphysics parameterization. Part IV: Sensitivity experiments. *J. Atmos. Sci.,* **63,** 3137–3159.

——, ——, J. Mailhot, and S. Bélair, 2008: Simulation of an orographic precipitation event during IMPROVE-2. Part I: Evaluation of the control run using a triple-moment bulk microphysics scheme. *Mon. Wea. Rev.,* **136,** 3873–3893.

——, R. McTaggart-Cowan, and D. Jacob, 2009: Forecasting the solid-to-liquid ratio of precipitation in a cloud-resolving model. Preprints, *23rd Conf. on Weather, Analysis, and Forecasting/19th Conf. on Numerical Weather Prediction,* Omaha, NE, Amer. Meteor. Soc., 7A2. [Available online at http://ams.confex.com/ams/pdfpapers/154287.pdf.]

Morrison, H., and J. O. Pinto, 2005: Mesoscale modeling of springtime arctic mixed-phase clouds using a new two-moment bulk microphpysics scheme. *J. Atmos. Sci.,* **62,** 3683–3704.

——, and ——, 2006: Intercomparison of bulk cloud microphysics schemes in mesoscale simulations of springtime arctic mixed-phase stratiform clouds. *Mon. Wea. Rev.,* **134,** 1880–1900.

——, and W. W. Grabowski, 2008: A novel approach for representing ice microphysics in models: Description and tests using a kinematic framework. *J. Atmos. Sci.,* **65,** 1528–1548.

——, J. A. Curry, and V. I. Khvorostyanov, 2005: A new double-moment microphysics parameterization for application in cloud and climate models. Part I: Description. *J. Atmos. Sci.,* **62,** 1665–1677.

——, J. O. Pinto, J. A. Curry, and G. M. McFarquhar, 2008: Sensitivity of modeled arctic mixed-phase stratocumulus to cloud condensation and ice nuclei over regionally varying surface conditions. *J. Geophys. Res.,* **113,** D05203, doi:10.1029/2007JD008729.

——, G. Thompson, and V. Tatarskii, 2009: Impact of cloud microphysics on the development of trailing stratiform precipitation in a simulated squall line: Comparison of one- and two-moment schemes. *Mon. Wea. Rev.,* **137,** 991–1007.

Murakami, M., 1990: Numerical modeling of dynamical and microphysical evolution of an isolated convective cloud—The 19 July CCOPE cloud. *J. Meteor. Soc. Japan,* **68,** 107–128.

Phillips, V. T. J., L. J. Donner, and S. T. Garner, 2007: Nucleation processes in deep convection simulated by a cloud-resolving model with double-moment bulk microphysics. *J. Atmos. Sci.,* **64,** 738–761.

Reisner, J., R. M. Rasmussen, and R. T. Bruintjes, 1998: Explicit forecasting of supercooled liquid water in winter storms using the MM5 mesoscale model. *Quart. J. Roy. Meteor. Soc.,* **124,** 1071–1107.

Rutledge, S. A., and P. V. Hobbs, 1983: The mesoscale and microscale structure and organization of clouds and precipitation in midlatitude cyclones. VII: A model for the "seeder-feeder" process in warm-frontal rainbands. *J. Atmos. Sci.,* **40,** 1185–1206.

Seifert, A., 2008: On the parameterization of evaporation of raindrops as simulated by a one-dimensional rainshaft model. *J. Atmos. Sci.,* **65,** 3608–3619.

——, and K. D. Beheng, 2001: A double-moment parameterization for simulating autoconversion, accretion and self-collection. *Atmos. Res.,* **59–60,** 265–281.

Skamarock, W. C., J. B. Klemp, J. Dudhia, D. O. Gill, D. M. Barker, W. Wang, and J. G. Powers, 2007: A description of the Advanced Research WRF version 2. NCAR Tech. Note NCAR/TN-468+STR, 88 pp.

Solomon, A., H. Morrison, P. O. G. Persson, M. D. Shupe, and J.-W. Bao, 2009: Investigation of microphysical parameterizations of snow and ice in Arctic clouds during M-PACE through model-observation comparisons. *Mon. Wea. Rev.,* **137,** 3110–3128.

van den Heever, S. C., and W. R. Cotton, 2004: The impact of hail size on simulated supercell storms. *J. Atmos. Sci.,* **61,** 1596–1609.

Van Weverberg, K., N. van Lipzip, and L. Delobbe, 2010: Evaluation of moist processes during intense precipitation in km-scale NWP models using remote sensing and in-situ data: Impact of microphysics size distribution assumptions. *Atmos. Res.,* **99,** 15–38.

Verlinde, H., and W. R. Cotton, 1993: Fitting microphysical observations of nonsteady convective clouds to a numerical model: An application of the adjoint technique of data assimilation to a kinematic model. *Mon. Wea. Rev.,* **121,** 2776–2793.

Walko, R. L., W. R. Cotton, M. P. Meyers, and J. Y. Harrington, 1995: New RAMS cloud microphysics parameterization. Part I: The single-moment scheme. *Atmos. Res.,* **38,** 29–62.

Weisman, M. L., and J. B. Klemp, 1982: The dependence of numerically simulated convective storms on vertical wind shear and buoyancy. *Mon. Wea. Rev.,* **110,** 504–520.

——, and ——, 1984: The structure and classification of numerically simulated convective storms in directionally varying wind shears. *Mon. Wea. Rev.,* **112,** 2479–2498.

——, and R. Rotunno, 2000: The use of vertical wind shear versus helicity in interpreting supercell dynamics. *J. Atmos. Sci.,* **57,** 1452–1472.

Ziegler, C. L., 1985: Retrieval of thermal and microphysical variables in observed convective storms. Part I: Model development and preliminary testing. *J. Atmos. Sci.,* **42,** 1487–1509.